



**HAL**  
open science

# Effects of nozzle-exit boundary-layer profile on the initial shear-layer instability, flow field and noise of subsonic jets

Christophe Bogey, Roberto Sabatini

► **To cite this version:**

Christophe Bogey, Roberto Sabatini. Effects of nozzle-exit boundary-layer profile on the initial shear-layer instability, flow field and noise of subsonic jets. *Journal of Fluid Mechanics*, 2019, 876, pp.288 - 325. 10.1017/jfm.2019.546 . hal-02333791

**HAL Id: hal-02333791**

**<https://hal.science/hal-02333791v1>**

Submitted on 24 Nov 2020

**HAL** is a multi-disciplinary open access archive for the deposit and dissemination of scientific research documents, whether they are published or not. The documents may come from teaching and research institutions in France or abroad, or from public or private research centers.

L'archive ouverte pluridisciplinaire **HAL**, est destinée au dépôt et à la diffusion de documents scientifiques de niveau recherche, publiés ou non, émanant des établissements d'enseignement et de recherche français ou étrangers, des laboratoires publics ou privés.

# Effects of nozzle-exit boundary-layer profile on the initial shear-layer instability, flow field and noise of subsonic jets

Christophe Bogey<sup>1†</sup> and Roberto Sabatini<sup>2</sup>

<sup>1</sup>Univ Lyon, Ecole Centrale de Lyon, INSA Lyon, Université Claude Bernard Lyon I, CNRS,  
Laboratoire de Mécanique des Fluides et d'Acoustique, UMR 5509, F-69134, Ecully, France

<sup>2</sup>Department of Physical Sciences, Embry-Riddle Aeronautical University,  
Daytona Beach, 32114 Florida, USA

(Received \*\*\*)

The influence of the nozzle-exit boundary-layer profile on high-subsonic jets is investigated by performing compressible large-eddy simulations (LES) for three isothermal jets at a Mach number of 0.9 and a diameter-based Reynolds number of  $5 \times 10^4$ , and by conducting linear stability analyses from the mean flow fields. At the exit section of a pipe nozzle, the jets exhibit boundary layers of momentum thickness of approximately 2.8% of the nozzle radius and a peak value of turbulence intensity of 6%. The boundary-layer shape factors, however, vary and are equal to 2.29, 1.96 and 1.71. The LES flow and sound fields differ significantly between the first jet with a laminar mean exit velocity profile and the two others with transitional profiles. They are close to each other in these two cases, suggesting that similar results would also be obtained for a jet with a turbulent profile. For the two jets with non-laminar profiles, the instability waves in the near-nozzle region emerge at higher frequencies, the mixing layers spread more slowly and contain weaker low-frequency velocity fluctuations, and the noise levels in the acoustic field are lower by 2-3 dB compared to the laminar case. These trends can be explained by the linear stability analyses. For the laminar boundary-layer profile, the initial shear-layer instability waves are most strongly amplified at a momentum-thickness-based Strouhal number  $St_\theta = 0.018$ , which is very similar to the value obtained downstream in the mixing-layer velocity profiles. For the transitional profiles, on the contrary, they predominantly grow at higher Strouhal numbers, around  $St_\theta = 0.026$  and  $0.032$ , respectively. As a consequence, the instability waves rapidly vanish during the boundary-layer/shear-layer transition in the latter cases, but continue to grow over a large distance from the nozzle in the former case, leading to persistent large-scale coherent structures in the mixing layers for the jet with a laminar exit velocity profile.

## 1. Introduction

There has been a considerable amount of studies on the effects of the initial conditions on free shear layers and jets for more than five decades. In particular, a great attention has been paid to the state of the nozzle-exit boundary layer, which may vary from one experiment to another depending on the facility characteristics and on the nozzle diameter and geometry. For instance, the jets are often initially laminar in small-scale experiments, whereas they are initially turbulent in full-scale experiments. In order to make meaningful comparisons, it can therefore be necessary to trip the boundary layer in

† Email address for correspondence: christophe.bogey@ec-lyon.fr

41 the nozzle in order to generate turbulent exit conditions, as was the case in the pioneering  
 42 work of Bradshaw (1966) and Crow & Champagne (1971).

43 The differences obtained between initially laminar and initially turbulent shear layers  
 44 and jets have been described in a long list of papers. In the laminar case, instability waves  
 45 are amplified just downstream of the nozzle at a preferred momentum-thickness-based  
 46 Strouhal number equal to  $St_\theta = 0.017$  according to the linear stability analyses conducted  
 47 from hyperbolic-tangent velocity profiles (Michalke 1984), and varying within the range  
 48  $0.009 \leq St_\theta \leq 0.018$  in experiments (Sato 1971; Zaman & Hussain 1981; Gutmark & Ho  
 49 1983). The shear layers subsequently roll up to form essentially two-dimensional vortical  
 50 structures, whose interactions result in three-dimensional turbulence. The levels of veloc-  
 51 ity fluctuations rapidly increase and reach a sharp peak during that laminar-turbulent  
 52 transition. In the initially turbulent case, on the contrary, they grow monotonically and  
 53 very slowly from the nozzle exit (Bradshaw 1966; Hill *et al.* 1976; Browand & Latigo  
 54 1979; Hussain & Zedan 1978*b*; Husain & Hussain 1979). Moreover, the jet flow devel-  
 55 opment is found to be faster in the laminar case than in the turbulent case, leading to  
 56 a shorter potential core and a higher rate of centerline velocity decay (Hill *et al.* 1976;  
 57 Raman *et al.* 1989, 1994; Russ & Strykowski 1993; Xu & Antonia 2002). The impact of  
 58 the nozzle-exit boundary-layer state is also significant on jet noise sources, as reported in  
 59 the review papers by Crighton (1981) and Lilley (1994). It has notably been established  
 60 in Maestrello & McDaid (1971), Zaman (1985*a,b*) and Bridges & Hussain (1987) that  
 61 initially laminar jets emit more noise than initially turbulent jets, and that the additional  
 62 acoustic components can be attributed to the pairings of the two-dimensional vortices  
 63 induced by the laminar-turbulent transition in the shear layers. After the transition,  
 64 coherent, well-organized turbulent structures appear to persist, as revealed by the exper-  
 65 iments of Brown & Roshko (1974) and Wygnanski *et al.* (1979). The presence of coherent  
 66 structures in initially turbulent mixing layers is less obvious according to Chandrsuda  
 67 *et al.* (1978), but is supported by the measurements in such flows of a peak Strouhal  
 68 number of  $St_\theta = 0.022 - 0.028$  by Drubka & Nagib (1981), Hussain & Zaman (1985) and  
 69 Morris & Foss (2003). The reasons for these values of Strouhal number well above those  
 70 obtained for initially laminar flow conditions remain however unexplained, as was noted  
 71 by Ho & Huerre (1984).

72 The issue of jet initial conditions has recently received renewed attention in the aeroa-  
 73 coustics community since Viswanathan (2004) stated that the jet far-field measurements  
 74 of Tanna (1977) might be contaminated by spurious facility noise. In reply to this, Harper-  
 75 Bourne (2010) suggested that the extra components emerging at high frequencies in  
 76 Tanna (1977)'s sound spectra are due to laminar flow conditions at the nozzle exit. This  
 77 seems to be confirmed by the experimental results obtained by Viswanathan & Clark  
 78 (2004), Zaman (2012) and Karon & Ahuja (2013) for high-subsonic jets exhausting from  
 79 two nozzles of different internal profiles, namely the ASME and the conical nozzles. In-  
 80 deed, more noise is measured with the ASME nozzle than with the conical nozzle, that  
 81 is, for highly-disturbed, nominally laminar boundary layers than for turbulent boundary  
 82 layers, refer to the nozzle-exit conditions of table 1. For instance, for the jet at a Mach  
 83 number of 0.896 considered by Zaman (2012), the sound levels with the ASME nozzle  
 84 are stronger by 2-3 dB for diameter-based Strouhal numbers  $St_D \geq 0.3$  at all radiation  
 85 angles, and approximately by 1 dB for lower frequencies at angles between 60 and 90  
 86 degrees with respect to the flow direction. On the basis of flow visualizations, Zaman  
 87 (2017) related this to the perseverance of organized coherent structures in the shear lay-  
 88 ers of the jets issuing from the ASME nozzle. Similarly, in the experiment of Fontaine  
 89 *et al.* (2015) who explored the shear-layer flow properties and the noise of three initially  
 90 highly disturbed jets with different nozzle-exit conditions, given in table 1, the jet from

reference	case	$Re_D$	H	$\delta_\theta/r_0$	$Re_\theta$	$u'_e/u_j$
Zaman (2012)	ASME, M = 0.37	$2.2 \times 10^5$	(laminar)	0.0050	556	11.5%
	conical, M = 0.37	$2.2 \times 10^5$	(turbulent)	0.0106	1179	7%
Karon & Ahuja (2013)	ASME, M = 0.40	$3.5 \times 10^5$	2.34	0.0049	870	-
	conical, M = 0.40	$3.5 \times 10^5$	1.71	0.0065	1135	-
Fontaine <i>et al.</i> (2015)	short nozzle	$6.6 \times 10^5$	2.18	0.0109	3620	14%
	medium nozzle	$6.6 \times 10^5$	1.53	0.0307	10180	13%
	long nozzle	$6.6 \times 10^5$	1.47	0.0426	14030	12%
Brès <i>et al.</i> (2018)	Baseline_LES_10M	$10^6$	2.54	0.0102	5100	6%
	BL16M_WM_Turb	$10^6$	1.55	0.0142	7100	13%
Morris & Foss (2003)	turb. boundary layer	-	1.31	-	4650	-

TABLE 1. Flow conditions at the nozzle exit for round jets (Zaman 2012; Karon & Ahuja 2013; Fontaine *et al.* 2015; Brès *et al.* 2018) and at the separation point created using a sharp edge for a turbulent boundary layer (Morris & Foss 2003).

91 the small nozzle with a partially developed boundary layer generates 3 dB more intense  
92 sound than the two jets from the medium and large nozzles with fully turbulent bound-  
93 ary layers. In addition, the peak turbulence intensities a few diameters downstream of  
94 the nozzle exit are stronger for the first jet.

95 The relative importance of each of the nozzle-exit parameters in the above results is  
96 difficult to distinguish, because these parameters usually vary simultaneously, as illus-  
97 trated in table 1. When the nozzle-exit flow conditions become turbulent, with or without  
98 boundary-layer tripping, the shape factor of the boundary-layer profile decreases. This  
99 factor, defined as  $H = \delta^*/\delta_\theta$  where  $\delta^*$  and  $\delta_\theta$  are the boundary-layer displacement and  
100 momentum thicknesses, takes values around 2.5 for laminar profiles and 1.4 for turbulent  
101 profiles. At the same time, the boundary-layer thickness increases, and the nozzle-exit  
102 peak turbulence intensities  $u'_e/u_j$ , where  $u'_e$  and  $u_j$  are the maximum rms value of ve-  
103 locity fluctuations and the jet velocity, most often grow. In some experiments, similar  
104 turbulence levels are obtained, as, for instance, in the work of Morris & Zaman (2009)  
105 where values of  $u'_e/u_j$  equal to 6.7% and 7.5% are reported for untripped and tripped  
106 jets at a diameter-based Reynolds number  $Re_D = 3 \times 10^5$ . It even happens that the  
107 velocity fluctuations are larger in laminar than in turbulent nozzle-exit boundary lay-  
108 ers. Examples of this counter-intuitive tendency have been given by Raman *et al.* (1989,  
109 1994) for tripped/untripped jets and by Zaman (2012) who measured values of  $u'_e/u_j$   
110 around 11% using the ASME nozzle but around 7% using the conical nozzle for jets at  
111  $2 \times 10^5 \leq Re_D \leq 6 \times 10^5$ , see the values for  $Re_D = 2.2 \times 10^5$  in table 1. In that case, the  
112 effects of the velocity profile and those of the turbulence levels are likely to counteract  
113 each other, which may result in some confusion.

114 Therefore, there is clearly a need to study the influence of the nozzle-exit boundary-  
115 layer profile with all other exit parameters held constant. For this, it seems worthwhile to  
116 use unsteady compressible simulations, which have made spectacular progress over the  
117 last three decades, and now allow us to conduct investigations under controlled condi-  
118 tions. Large-eddy simulations (LES) have for instance been run by the first author over  
119 the last decade (Bogey & Bailly 2010; Bogey *et al.* 2011*b,c*, 2012*a,b*; Bogey & Marsden  
120 2013; Bogey 2018) to investigate the impact of nozzle-exit conditions on initially laminar  
121 and highly-disturbed subsonic round jets. Due to limitations in computing resources,  
122 the jets had moderate Reynolds numbers  $Re_D$  between  $2.5 \times 10^4$  and  $2 \times 10^5$ , and all

123 exhibited laminar mean velocity profiles at the nozzle exit, in order to ensure numerical  
 124 accuracy. Subsonic jets with tripped boundary layers have also been recently calculated  
 125 by an increasing number of other researchers, including Lorteau *et al.* (2015) and Zhu  
 126 *et al.* (2018), among others. Specifically concerning initially turbulent jets, the first at-  
 127 tempts of computation have been made by Bogey *et al.* (2008) and Uzun & Hussaini  
 128 (2007). However, the grid was too coarse in the former case, while its spatial extent was  
 129 limited to 4.5 diameters downstream of the nozzle in the latter. Later, Sandberg *et al.*  
 130 (2012) carried out the simulation of a fully turbulent pipe flow at  $Re_D = 7,500$  exiting  
 131 into a coflow, and Bühler *et al.* (2014) successfully computed a jet at  $Re_D = 18,100$  with  
 132 turbulent conditions at the exit of a pipe nozzle. None of these studies however addresses  
 133 the question of the mean velocity profile. More recently, two jets at  $Re_D = 2 \times 10^5$  with  
 134 nozzle-exit conditions roughly matching those found in experiments using the ASME and  
 135 the conical nozzles have been performed by Bogey & Marsden (2016). Unfortunately, the  
 136 results for the two jets are very similar, suggesting that the jet initial conditions in the  
 137 simulations do not adequately reflect those in the experiments. Finally, Brès *et al.* (2018)  
 138 calculated two isothermal subsonic jets at  $Re_D = 10^6$  with initially laminar and turbu-  
 139 lent nozzle-exit boundary layers, as indicated in table 1. The initially laminar jet radiates  
 140 greater high-frequency noise than the initially turbulent jet, which was attributed to the  
 141 fact that the instability waves in the near-nozzle region grow at different rates in the two  
 142 jets.

143 In the present work, the influence of the nozzle-exit boundary-layer profile on high-  
 144 subsonic jets is investigated by combining well-resolved large-eddy simulations and linear  
 145 stability analyses for three isothermal round jets at a Mach number  $M = u_j/c_a = 0.9$   
 146 and a Reynolds number  $Re_D = u_j D/\nu = 5 \times 10^4$ , where  $c_a$ ,  $D$  and  $\nu$  are the speed of  
 147 sound in the ambient medium, the jet diameter and the kinematic molecular viscosity. In  
 148 order to consider the effects of the mean velocity profile alone, momentum boundary-layer  
 149 thicknesses of  $\delta_\theta \simeq 0.028r_0$  and peak turbulence intensities of  $u'_e/u_j \simeq 6\%$  are prescribed  
 150 at the exit of a pipe nozzle for all jets. The boundary-layer profiles however vary, and  
 151 are laminar in the first jet and transitional (partially developed) in the two others, with  
 152 shape factors  $H$  ranging between 1.71 and 2.29. The first objective will be to determine  
 153 whether the flow and sound fields of the jets show significant differences, and whether  
 154 these differences correspond to those usually encountered between initially laminar and  
 155 initially turbulent jets, namely a faster flow development, stronger velocity fluctuations in  
 156 the mixing layers and more noise in the acoustic field in the laminar case. In particular,  
 157 comparisons will be made with the trends observed in the experiments of Zaman (2012,  
 158 2017) using the ASME and the conical nozzles and of Fontaine *et al.* (2015), and in the  
 159 simulations of Brès *et al.* (2018). They will be mostly qualitative due to the disparities in  
 160 upstream flow conditions. The second objective will be to propose an explanation for the  
 161 higher noise levels expected for a laminar boundary-layer profile. For that purpose, the  
 162 development of the instability waves very near the nozzle exit and during the transition  
 163 from a boundary layer to a shear layer will be detailed. It will also be discussed based  
 164 on the linear stability analyses conducted from the mean flow fields, as in Fontaine *et al.*  
 165 (2015) and Brès *et al.* (2018). However, while the latter authors mainly focused on the  
 166 amplification rates of the instability waves, the present study will specially examine the  
 167 sensitivity of the unstable frequencies to the nozzle-exit velocity profile, previously noted  
 168 by Drubka & Nagib (1981), Hussain & Zaman (1985) and Morris & Foss (2003) for shear  
 169 layers, and its possible role in the discrepancies observed in the flow and sound fields of  
 170 the jets.

171 The paper is organized as follows. The parameters of the three jets, of the large-  
 172 eddy simulations, of the extrapolations of the LES acoustic near fields to the far field

---

	H	$\delta_\theta/r_0$	$\delta_{99}/r_0$	$\alpha_{trip}$
jetBL	2.55	0.0288	0.202	0.0460
jetT1	1.88	0.0288	0.215	0.0675
jetT2	1.52	0.0288	0.254	0.0830

---

TABLE 2. Shape factor H, momentum thickness  $\delta_\theta$  and 99% velocity thickness  $\delta_{99}$  of the boundary-layer profile at the pipe-nozzle inlet, and strength of the trip-like excitation  $\alpha_{trip}$ .

---

173 and of the linear stability analyses are documented in section 2. The nozzle-exit flow  
 174 properties, the mixing-layer and jet flow fields, and the jet acoustic fields are described  
 175 in section 3. Concluding remarks are given in section 4. Finally, comparisons of the non-  
 176 laminar nozzle-inlet velocity profiles imposed for two of the three jets with boundary-layer  
 177 measurements are shown in appendix A, and results from a grid-refinement study are  
 178 provided in appendix B.

## 179 2. Parameters

### 180 2.1. Jet definition

181 Three isothermal round jets at a Mach number  $M = 0.9$  and a Reynolds number  $Re_D =$   
 182  $5 \times 10^4$ , referred to as jetBL, jetT1 and jetT2 in what follows, have been simulated. They  
 183 originate at  $z = 0$  from a pipe nozzle of radius  $r_0$  and length  $2r_0$ , whose lip is  $0.053r_0$   
 184 thick, into a medium at rest of temperature  $T_a = 293$  K and pressure  $p_a = 10^5$  Pa. At the  
 185 pipe inlet, at  $z = -2r_0$ , different boundary-layer profiles, whose main characteristics are  
 186 collected in table 2, are imposed for the axial velocity. Radial and azimuthal velocities are  
 187 set to zero, pressure is equal to  $p_a$ , and temperature is determined by a Crocco-Busemann  
 188 relation.

The inlet axial velocity profiles are represented in figure 1(a). In jetBL, the profile is a  
 Blasius laminar boundary-layer profile with a shape factor  $H = \delta^*/\delta_\theta = 2.55$ , where the  
 boundary-layer displacement and momentum thicknesses are respectively defined as

$$\delta^* = \int_0^\infty \left( 1 - \frac{\langle u_z \rangle}{\langle u_z \rangle(r=0)} \right) dr$$

and

$$\delta_\theta = \int_0^\infty \frac{\langle u_z \rangle}{\langle u_z \rangle(r=0)} \left( 1 - \frac{\langle u_z \rangle}{\langle u_z \rangle(r=0)} \right) dr$$

The Blasius profile is given by the Pohlhausen's fourth-order polynomial approximation

$$\frac{u_{inlet}(r)}{u_j} = \begin{cases} \frac{(r_0 - r)}{\delta_{BL}} \left[ 2 - 2 \left( \frac{(r_0 - r)}{\delta_{BL}} \right)^2 + \left( \frac{(r_0 - r)}{\delta_{BL}} \right)^3 \right] & \text{if } r \geq r_0 - \delta_{BL} \\ 1 & \text{otherwise} \end{cases} \quad (2.1)$$

189 where  $\delta_{BL}$  is the boundary-layer thickness.

In jetT1 and jetT2, the inlet profiles are transitional boundary-layer profiles with  
 $H = 1.88$  and  $H = 1.52$ , respectively. They are derived from the turbulent profile proposed  
 by De Chant (2005), and defined as

$$\frac{u_{inlet}(r)}{u_j} = \begin{cases} \left( \sin \left[ \frac{\pi}{2} \left( \frac{r_0 - r}{\delta_{T_i}} \right)^{\beta_i} \right] \right)^{\gamma_i} & \text{if } r \geq r_0 - \delta_{T_i} \\ 1 & \text{otherwise} \end{cases} \quad (2.2)$$

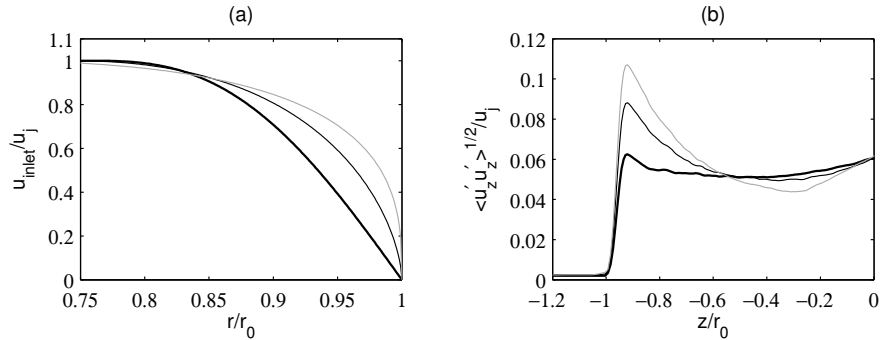


FIGURE 1. Representation (a) of the axial velocity profile  $u_{inlet}$  imposed at the pipe-nozzle inlet and (b) of the peak rms values of axial velocity fluctuations  $u'_z$  in the nozzle: — jetBL, - - - jetT1, ··· jetT2.

190 where  $\delta_{T_i}$  is the boundary-layer thickness, and the values of the exponents  $\beta_i$  and  $\gamma_i$   
 191 are equal to  $\beta_1 = 0.464$  and  $\gamma_1 = 1.32$ , and to  $\beta_2 = 0.423$  and  $\gamma_2 = 0.82$ . Considering  
 192 the strong similarities between the near-wall mean-flow statistics obtained for turbulent  
 193 pipe and boundary layer flows (Monty *et al.* 2009), they have been designed to fit the  
 194 experimental data provided by Schubauer & Klebanoff (1955) for a flat-plate boundary  
 195 layer in the region of changeover from laminar to fully turbulent conditions, as shown in  
 196 appendix A.

197 In the three jets, the inlet boundary-layer thicknesses are arbitrarily set to  $\delta_{BL} = 0.25r_0$   
 198 in jetBL,  $\delta_{T_1} = 1.043\delta_{BL} = 0.26r_0$  in JetT1 and  $\delta_{T_2} = 1.328\delta_{BL} = 0.33r_0$  in JetT2, in  
 199 order to obtain a momentum thickness of  $\delta_\theta = 0.0288r_0$  in all cases. The associated 99%  
 200 velocity thicknesses  $\delta_{99}$  thus vary from  $0.202r_0$  in jetBL up to  $0.254r_0$  in jetT2. With  
 201 respect to the experiments of Zaman (2012) and Karon & Ahuja (2013), see in table 1, the  
 202 boundary layers in the present jets are thicker to guarantee a high numerical accuracy,  
 203 as will be discussed in section 2.3 and in appendix B. Given the jet Reynolds number of  
 204  $Re_D = 5 \times 10^4$ , chosen to perform very well resolved LES, this also leads to a momentum-  
 205 thickness-based Reynolds number of  $Re_\theta = u_j \delta_\theta / \nu = 720$ , which is comparable to the  
 206 values measured in the experiments. This is of importance because  $Re_\theta$  is a key parameter  
 207 in developing shear layers (Hussain & Zedan 1978*b*; Bogey & Marsden 2013).

208 In order to generate disturbed upstream conditions for the jets, which otherwise would  
 209 initially contain negligible velocity fluctuations, the boundary layers are 'tripped' in the  
 210 pipe using an arbitrary forcing devices whose parameters are determined by trial and  
 211 error (Klebanoff & Diehl 1952; Coles 1962; Erm & Joubert 1991; Schlatter & Örlü 2012;  
 212 Hutchings 2012; Castillo & Johansson 2012). In simulations, forcing devices of different  
 213 kinds have been proposed. A small step can for instance be mounted on the wall inside the  
 214 nozzle. Random fluctuations, synthetic turbulence or instability modes can alternatively  
 215 be imposed on the flow profiles. In the present jets, the forcing procedure detailed in  
 216 the appendix A of Bogey *et al.* (2011*b*) is implemented. It consists in adding random  
 217 low-level vortical disturbances uncorrelated in the azimuthal direction in the boundary  
 218 layers. It has been previously used for both laminar (Bogey *et al.* 2011*b*, 2012*b,a*; Bogey  
 219 & Marsden 2013) and non-laminar (Bogey & Marsden 2016) boundary-layer profiles.  
 220 The forcing is applied at the axial position  $z = -0.95r_0$  and at the radial position  
 221 of  $r = r_0 - \delta_{BL}/2 = 0.875r_0$  in all cases. However, the forcing magnitudes are not  
 222 the same, and have been adjusted after preliminary tests to obtain peak nozzle-exit  
 223 turbulence intensities  $u'_e/u_j$  of 6% for all jets. This level is close to those measured by  
 224 Zaman (2012) just downstream of the conical nozzle for initially turbulent jets, refer to

225 table 1 for instance. The values of the coefficient  $\alpha_{trip}$  setting the maximum value of the  
 226 added velocity fluctuations to  $\alpha_{trip}u_j$ , hence specifying the forcing strength, are given in  
 227 table 2. They are equal to 0.046, 0.0675 and 0.083 in jetBL, jetT1 and jetT2, respectively.  
 228 Consequently, the lower the inlet boundary-layer shape factor, the higher the amplitude  
 229 of the excitation necessary to reach  $u'_e/u_j = 6\%$ . This is illustrated in figure 1(b) showing  
 230 the variations of the maximum rms value of axial velocity fluctuations in the pipe.

231 As pointed out above, there exit some discrepancies between the nozzle-exit conditions  
 232 of the present jets and of the experiments of table 1 in terms of  $Re_D$  and ratio  $\delta_\theta/r_0$ .  
 233 The higher value of  $\delta_\theta/r_0$  in the simulations, in particular, will result in lower frequencies  
 234 in the shear layers just downstream of the nozzle. Thanks to the similarities in  $Re_\theta$  and  
 235  $u'_e/u_j$ , the physical mechanisms at play in this zone can yet be expected to be of the  
 236 same nature as those in the experiments using the ASME and conical nozzles. Performing  
 237 qualitative comparisons with the trends revealed in these experiments therefore appears  
 238 relevant. Quantitative comparisons with measurements for reference jets of the literature  
 239 will also be made throughout the paper. They are given mainly for illustration purposes,  
 240 because these jets have Reynolds numbers  $Re_D \simeq 10^6$  and certainly very thin nozzle-exit  
 241 boundary layers. In addition, they are most likely initially fully turbulent, and such a case  
 242 is not considered in this study. It is however hoped that on the basis of the differences  
 243 obtained between jetT1 and jetT2, results for a more turbulent boundary-layer profile  
 244 could be extrapolated. Finally, the experimental jets all exhaust for a convergent nozzle,  
 245 leading to a pressure gradient at the nozzle exit whose effects are unclear (Zaman 2012),  
 246 which is not taken into account in the simulations.

## 2.2. LES numerical methods

247  
 248 For the LES, the numerical framework is identical to that used in previous jet simula-  
 249 tions (Bogey & Bailly 2010; Bogey *et al.* 2012*b*, 2011*b*, 2012*a*; Bogey & Marsden 2013;  
 250 Bogey 2018). They are carried out using an in-house solver of the three-dimensional fil-  
 251 tered compressible Navier-Stokes equations in cylindrical coordinates  $(r, \theta, z)$  based on  
 252 low-dissipation and low-dispersion explicit schemes. The axis singularity is taken into  
 253 account by the method of Mohseni & Colonius (2000). In order to alleviate the time-step  
 254 restriction near the cylindrical origin, the derivatives in the azimuthal direction around  
 255 the axis are calculated at coarser resolutions than permitted by the grid (Bogey *et al.*  
 256 2011*a*). For the points closest to the jet axis, they are evaluated using 16 points, yield-  
 257 ing an effective resolution of  $2\pi/16$ . Fourth-order eleven-point centered finite differences  
 258 are used for spatial discretization, and a second-order six-stage Runge-Kutta algorithm  
 259 is implemented for time integration (Bogey & Bailly 2004). A sixth-order eleven-point  
 260 centered filter (Bogey *et al.* 2009*b*) is applied explicitly to the flow variables every time  
 261 step. Non-centered finite differences and filters are also used near the pipe walls and the  
 262 grid boundaries (Berland *et al.* 2007; Bogey & Bailly 2010). At the boundaries, the radi-  
 263 ation conditions of Tam & Dong (1996) are applied, with the addition at the outflow of a  
 264 sponge zone combining grid stretching and Laplacian filtering (Bogey & Bailly 2002). At  
 265 the inflow and radial boundaries, density and pressure are also brought back close to  $p_a$   
 266 and  $\rho_a$  every  $0.055r_0/c_a$  at rate of 0.5%, in order to keep the mean values of density and  
 267 pressure around their ambient values without generating significant acoustic reflections.  
 268 No co-flow is imposed.

269 In the present large-eddy simulations, the explicit filtering is employed to remove grid-  
 270 to-grid oscillations, but also as a subgrid-scale high-order dissipation model in order to  
 271 relax turbulent energy from scales at wave numbers close to the grid cut-off wave number  
 272 while leaving larger scales mostly unaffected. The performance of this LES approach has  
 273 been assessed in past studies for subsonic jets, Taylor-Green vortices and turbulent chan-



---

$n_r \times n_\theta \times n_z$	$\Delta r/r_0$	$(r_0\Delta\theta)/r_0$	$\Delta z/r_0$	$L_r/r_0$	$L_z/r_0$	$Tu_j/r_0$
$504 \times 1024 \times 2085$	0.36%	0.61%	0.72%	15	40	500

---

TABLE 3. Numbers of grid points  $n_r$ ,  $n_\theta$  and  $n_z$ , mesh spacings  $\Delta r$  at  $r = r_0$ ,  $r_0\Delta\theta$  and  $\Delta z$  at  $z = 0$ , extents of the physical domain  $L_r$  and  $L_z$ , and simulation time  $T$  after the transient period.

---

nel flows (Bogey *et al.* 2011*b*; Bogey & Bailly 2006, 2009; Fauconnier *et al.* 2013; Kremer & Bogey 2015), from comparisons with the solutions of direct numerical simulations and from the examination of the magnitude and the properties of the filtering dissipation in the wavenumber space.

### 2.3. Simulation parameters

The grid used in the present jet simulations is detailed and referred to as gridz40B in a recent grid-sensitivity study of the flow and acoustic fields of an initially highly disturbed isothermal round jet at  $M = 0.9$  and  $\text{Re}_D = 10^5$  (Bogey 2018). As indicated in table 3, it contains  $n_r \times n_\theta \times n_z = 504 \times 1024 \times 2048 = 10^9$  points. It extends radially out to  $L_r = 15r_0$  and axially, excluding the 100-point outflow sponge zone, down to  $L_z = 40r_0$ . There are 169 points along the pipe nozzle between  $z = -2r_0$  and  $z = 0$ , 96 points between  $r = 0$  and  $r = r_0$ , and 41 points between  $r = r_0 - \delta_{BL} = 0.75r_0$  and  $r = r_0$ . In the radial direction, the mesh spacing  $\Delta r$  is minimum and equal to  $0.0036r_0$  at  $r = r_0$ , and is equal to  $0.0141r_0$  at  $r = 0$ ,  $0.0148r_0$  at  $r = 2r_0$ ,  $0.0335r_0$  at  $r = 4r_0$  and  $0.075r_0$  between  $r = 6.25r_0$  and  $r = L_r$ . The latter mesh spacing leads to a diameter-based Strouhal number of  $\text{St}_D = fD/u_j = 5.9$  for an acoustic wave discretized by five points per wavelength, where  $f$  is the frequency. In the axial direction, the mesh spacing  $\Delta z$  is minimum and equal to  $0.0072r_0$  between  $z = -r_0$  and  $z = 0$ , and increases at a stretching rate of 0.103% farther downstream to reach  $0.0127r_0$  at  $z = 5r_0$ ,  $0.0178r_0$  at  $z = 10r_0$ ,  $0.0230r_0$  at  $z = 15r_0$  and  $0.0488r_0$  at  $z = L_z$ .

The quality of gridz40B has been shown in Bogey (2018) for a jet at  $\text{Re}_D = 10^5$  characterized, at the nozzle exit, by a laminar Blasius boundary layer of thickness  $\delta_{BL} = 0.25r_0$  and a peak turbulence intensity of  $u'_e/u_j = 9\%$ . Therefore, it is highly likely that in the present work, the grid resolution is appropriate for jetBL at  $\text{Re}_D = 5 \times 10^4$  with  $\delta_{BL} = 0.25r_0$  and  $u'_e/u_j = 6\%$ . For jetT1 and jetT2 with non-laminar boundary-layer profiles, the suitability of the grid is less obvious. In order to address this issue, the near-wall mesh spacings in the pipe expressed in wall units based on the wall friction velocity at the nozzle exit are provided in table 4. They are such that  $\Delta r^+ \leq 2.7$ ,  $(r_0\Delta\theta)^+ \leq 4.6$  and  $\Delta z^+ \leq 5.4$ . The azimuthal and axial mesh spacings meet the requirements needed to compute turbulent wall-bounded flows accurately using direct numerical simulation (Kim *et al.* 1987; Spalart 1988) or LES involving relaxation filtering (Gloerfelt & Berland 2012; Kremer & Bogey 2015). On the contrary, the wall-normal spacing is two or three times larger than the recommended value of  $\Delta r^+ = 1$ . For the simulation of an initially fully turbulent jet, refining the wall-normal region by a factor of at least three would therefore be necessary, which would increase by the same amount the computational cost due to the explicit time-integration scheme. For the initially transitional jets considered in this paper, the sensitivity to the wall-normal spacing has however been assessed in a preliminary study using two shorter grids extending axially, excluding the outflow sponge zones, only down to  $z = 4r_0$  in order to save computational time. The coarsest of the two grids coincides with gridz40B in the boundary-layer region. The finest one is also identical to the latter in that region in the directions  $\theta$  and  $z$ , but differs in the radial direction

---

	$\Delta r^+$	$(r_0\Delta\theta)^+$	$\Delta z^+$
JetBL	1.4	2.4	2.8
JetT1	2.1	3.6	4.3
JetT2	2.7	4.6	5.4

---

TABLE 4. Near-wall mesh spacings  $\Delta r$ ,  $r_0\Delta\theta$  and  $\Delta z$  given in wall units based on the wall friction velocity  $u_\tau$  at the nozzle exit.

---

315 with  $\Delta r/r_0 = 0.18\%$ , instead of  $\Delta r/r_0 = 0.36\%$ , at  $r = r_0$ . The tripping procedure is  
316 exactly the same in all cases, but the time step is twice as small in the LES using the  
317 finest grid because of the numerical stability condition, leading to an application of the  
318 relaxation filtering that is twice as frequent. The mean and fluctuating velocity profiles  
319 obtained at the nozzle exit using the two grids, represented in Appendix B for jetT2, are  
320 superimposed. This demonstrates that the LES solutions in the pipe do not depend on  
321 the radial mesh spacing at  $r = r_0$  or on the relaxation filtering.

322 In the three jet LES, the time step is defined by  $\Delta t = 0.7 \times \Delta r(r = r_0)/c_a$ , yielding  
323  $\Delta t = 0.0023 \times r_0/u_j$ . After a transient period of  $275r_0/u_j$ , the simulation time  $T$ , given  
324 in table 3, is equal to  $500r_0/u_j$ . During that time period, the signals of density, velocities  
325 and pressure obtained on the jet axis at  $r = 0$ , on the cylindrical surfaces located at  $r = r_0$   
326 and  $r = L_r = 15r_0$  and in the cross sections at  $z = -1.5r_0$ ,  $z = 0$  and  $z = L_z = 40r_0$ ,  
327 are recorded at a sampling frequency allowing spectra to be computed up to  $St_D = 12.8$ .  
328 The signals obtained in the four azimuthal planes at  $\theta = 0, \pi/4, \pi/2$  and  $3\pi/4$  are  
329 also stored, but at a halved frequency in order to reduce storage requirements. Finally,  
330 the Fourier coefficients estimated over the full section  $(r, z)$  for the first nine azimuthal  
331 modes for density, velocities and pressure are similarly saved. The flow and acoustic near  
332 field statistics presented in the next sections are calculated from these recordings. They  
333 are averaged in the azimuthal direction, when possible. Time spectra are evaluated from  
334 overlapping samples of duration  $45r_0/u_j$  on the jet axis, and  $90r_0/u_j$  otherwise. In the  
335 azimuthal direction, post-processing can be performed up to the mode  $n_\theta = 128$ , where  
336  $n_\theta$  is the dimensionless azimuthal wave number such that  $n_\theta = k_\theta r$ .

337 Finally, the simulations required 200 GB of memory and have run during 340,000  
338 iterations each. They have been performed using an OpenMP-based in-house solver on  
339 single nodes with 256 GB of memory, consisting of four Intel Sandy Bridge E5-4650 8-  
340 core processors at a clock speed of 2.7 GHz or of two Intel Xeon CPU E5-2670v3 8-core  
341 processors at 2.6 GHz. The time per iteration is approximately equal to 120 seconds in the  
342 first case using 32 cores and to 140 seconds in the second case using 16 cores, leading to  
343 the consumption of 1,070 and 620 CPU hours, respectively, for 1,000 iterations. Therefore,  
344 a total number of the order of 1 billion computational hours has been necessary for the  
345 full study.

#### 346 2.4. Linear stability analysis

347 Inviscid spatial stability analyses have been carried out from the mean flow fields of the  
348 jets, as was done in previous investigations (Fontaine *et al.* 2015; Brès *et al.* 2018). More  
349 precisely, the compressible Rayleigh equation (Michalke 1984; Sabatini & Bailly 2015)  
350 has been solved for the LES profiles of mean axial velocity and mean density, locally  
351 considered parallel, from  $z = 0.02r_0$  down to  $z = 5r_0$ . Viscous effects are not taken into  
352 account because they are expected to be very weak at the Reynolds numbers  $Re_\theta \gtrsim 700$   
353 considered in this work (Morris 1976, 2010). For a given axial distance  $z$  and a given  
354 Strouhal number  $St_D$ , the compressible Rayleigh equation is solved through a shooting

355 technique (Morris 2010), based on the Euler method for the integration step and on  
 356 the secant method for the search of the complex wavenumber  $k_z \delta_\theta$ . The integration is  
 357 performed on a grid with a spatial step of  $0.0001r_0$ , extending from the LES grid point  
 358 closest to the jet axis at  $r = 0.007r_0$  out to  $r = 5r_0$ . Since the present stability study is  
 359 performed directly from the LES profiles, which may contain high-frequency noise in the  
 360 near-nozzle region of high mean-flow gradients, the profiles and their radial derivatives  
 361 are filtered using a sixth-order eleven-point centered filter (Bogey *et al.* 2009b). A cubic  
 362 spline interpolation is then employed to calculate the mean-flow values on the aforesaid  
 363 grid. It can be noted that, in order to check the sensitivity of the results to the filtering,  
 364 a tenth-order eleven-point centered filter has also been used to smooth the LES profiles  
 365 of jetT2, in the case which exhibits the strongest gradients. The eigenvalues  $k_z \delta_\theta$  thus  
 366 obtained are identical to those calculated using the sixth-order filter.

### 367 2.5. Far-field extrapolation

368 The LES near-field fluctuations have been propagated to the far field using an in-house  
 369 OpenMP-based solver of the isentropic linearized Euler equations (ILEE) in cylindrical  
 370 coordinates, based on the same numerical methods as the LES (Bogey *et al.* 2009a; Bogey  
 371 2018). The extrapolations are carried out from the velocity and pressure fluctuations  
 372 recorded on the cylindric surface at  $r = L_r = 15r_0$  and on the axial sections at  $z = -1.5r_0$   
 373 and  $z = L_z = 40r_0$  over a time period of  $500r_0/u_j$  during the jet simulations, at a  
 374 sampling frequency corresponding to  $St_D = 12.8$ . They aim to provide the pressure waves  
 375 radiated at a distance of  $150r_0$  from the nozzle exit, where far-field acoustic conditions  
 376 are expected to apply according to measurements (Ahuja *et al.* 1987; Viswanathan 2006),  
 377 between the angles of  $\phi = 15^\circ$  and  $\phi = 165^\circ$  relative to the jet direction.

378 In practice, in order to compute separately the downstream and the upstream acoustic  
 379 fields, whose magnitudes strongly vary, two far-field extrapolations are performed on two  
 380 different grids, yielding results for  $15^\circ \leq \phi \leq 90^\circ$  and for  $60^\circ \leq \phi \leq 165^\circ$ , respectively.  
 381 The two grids are identical in the radial and the azimuthal directions, with  $n_r = 2058$  and  
 382  $n_\theta = 256$ . In the direction  $r$ , they extend from  $r = 2.5r_0$  out to  $r = 151r_0$  with a mesh  
 383 spacing of  $\Delta r = 0.075r_0$ , and end with a 80-point sponge zone. In the axial direction, the  
 384 two grids respectively contain  $n_z = 2171$  and  $n_z = 3111$  points, and extend, excluding  
 385 the 80-point sponge zones implemented at the upstream and downstream boundaries,  
 386 from  $z = -6r_0$  up to  $z = 146r_0$  and from  $z = -146r_0$  up to  $z = 76r_0$ , with a mesh  
 387 spacing of  $\Delta z = 0.075r_0$ . This mesh spacing, leading to a Strouhal number  $St_D = 5.9$   
 388 for an acoustic wave discretized by five points per wavelength, is identical to that in the  
 389 LES near field.

390 In the first computation, the LES fluctuations are imposed onto the extrapolation grid  
 391 for  $-1.5r_0 \leq z \leq L_z$  at  $r = L_r = 15r_0$ , for  $2.5r_0 \leq r \leq L_r$  at  $z = -1.5r_0$  and for  $7.5r_0 \leq$   
 392  $r \leq L_r$  at  $z = L_z = 40r_0$ . The opening angle relative to the flow direction, with the nozzle  
 393 exit as origin, is of  $\phi = 10^\circ$ , which allows most of the downstream noise components to  
 394 be taken into account. In the second computation, the LES data are imposed onto the  
 395 extrapolation grid as in the first one at  $z = -1.5r_0$  and at  $r = L_r = 15r_0$ , but only  
 396 for  $14r_0 \leq r \leq L_r$  at  $z = L_z = 40r_0$ . The opening angle is larger than in the first case  
 397 in order to avoid the presence of aerodynamic disturbances (Arndt *et al.* 1997) on the  
 398 extrapolation surface, which might cause low-frequency spurious waves (Bogey & Bailly  
 399 2010) in the upstream direction where noise levels are much lower than in the downstream  
 400 direction.

401 Each ILEE computation requires 105 or 150 GB of memory depending on the grid used,  
 402 and lasts during 7,700 iterations. This leads to a total number approximately of 25,000  
 403 CPU hours consumed using 16-core nodes based on Intel Xeon CPU E5-2670 processors

404 at 2.6 GHz. Finally, the far-field spectra are evaluated from the pressure signals obtained  
 405 at  $150r_0$  from the nozzle exit during the final 6,000 iterations of the computations, *i.e.*  
 406 during nearly  $470r_0/u_j$ . Thus, for the peak Strouhal number of  $St_D = 0.2$  emerging in the  
 407 downstream direction, and for the lowest Strouhal number of  $St_D = 0.075$  represented  
 408 in section 3.4.2, the far-field signals contains 48 and 18 time periods, respectively. The  
 409 statistical convergence of the results is furthermore increased by calculating the spec-  
 410 tra using overlapping samples of duration  $90r_0/u_j$ , and by averaging in the azimuthal  
 411 direction.

### 412 3. Results

#### 413 3.1. Jet flow initial conditions

##### 414 3.1.1. Nozzle-exit boundary-layer properties

415 The profiles of mean and rms axial velocities calculated at the nozzle exit are pre-  
 416 sented in figure 2. Their main properties are provided in table 5. In figure 2(a), as  
 417 intended, the mean velocity profiles differ significantly, and have shape factors  $H$  of 2.29  
 418 for jetBL, 1.96 for jetT1 and 1.71 for jetT2. The boundary-layer momentum thicknesses  
 419 are similar, and range only from  $\delta_\theta = 0.0299r_0$  for jetBL down to  $\delta_\theta = 0.0274r_0$  for  
 420 jetT2, leading to Reynolds numbers  $Re_\theta$  between 685 and 747. From jetBL to jetT2,  
 421 in addition, the 99% velocity thickness  $\delta_{99}$  increases slightly and the vorticity thickness  
 422  $\delta_\omega = \langle u_z \rangle(r=0) / \max(|\partial \langle u_z \rangle / \partial r|)$  evaluated from the maximum value of velocity gradi-  
 423 ent strongly decreases from  $\delta_\omega = 0.118r_0$  down to  $\delta_\omega = 0.043r_0$ . The mean velocity profile  
 424 for jetBL corresponds to a laminar boundary-layer profile, and, given that  $H \simeq 1.45$  is  
 425 obtained (Spalart 1988; Erm & Joubert 1991; Fernholz & Finley 1996; Schlatter & Örlü  
 426 2012) for fully developed boundary layers at  $Re_\theta = 700$ , the profiles for jetT1 and jetT2  
 427 are both transitional.

428 In figure 2(b), the peak turbulence intensities, imposed by the boundary-layer forcing,  
 429 are all close to  $u'_e/u_j = 6.1\%$ . They are reached roughly at the positions of the maximum  
 430 velocity gradients, hence move nearer to the wall from  $r_e = 0.935r_0$  for jetBL up to  $r_e =$   
 431  $0.975r_0$  for jetT2, as reported in table 5. The radial profile of rms velocity also changes  
 432 with the boundary-layer shape. In the non-laminar cases, compared to the laminar case  
 433 (Zaman 1985*a,b*), the peak is sharper and resembles that obtained in the inner region of  
 434 turbulent boundary layers (Spalart 1988; Schlatter & Örlü 2012) as well as that measured  
 435 just downstream of the nozzle lip for such flows (Morris & Foss 2003; Fontaine *et al.* 2015).

436 With respect to the parameters of the inlet boundary layers in table 2, the nozzle-  
 437 exit parameters in table 5 are slightly different due to the flow development in the pipe  
 438 between the forcing at  $z = -0.95r_0$  and the exit at  $z = 0$ . The boundary layer has a  
 439 lower shape factor and a larger momentum thickness at the exit than at the pipe inlet  
 440 for jetBL, whereas the opposite trends are observed for the two other jets.

441 The profiles of the skewness and kurtosis factors of the axial velocity fluctuations at  
 442  $z = 0$  are depicted in figure 3. As expected, significant deviations from the values of 0  
 443 and 3 are found in the interfaces between the laminar inner-pipe region and the highly  
 444 disturbed boundary layers, around  $r = 0.75r_0$ . They are stronger, in absolute value, as  
 445 the mean velocity profile has a more turbulent shape, and indicate the occurrence of  
 446 intermittent bursts of low-velocity fluid. In the boundary layers, the strongest deviations  
 447 are obtained for the laminar case, close to the wall as well as on the high-speed side of  
 448 the boundary layers. For instance, at  $r = r_0 - \delta_{94} = 0.827r_0$  where  $\delta_{94}$  is the 94% velocity  
 449 boundary-layer thickness, equal to  $0.173r_0$  for all jets, the skewness values are of  $-0.65$   
 450 for JetBL,  $-0.43$  for JetT1 and  $-0.28$  for JetT2. This tendency is in agreement with that

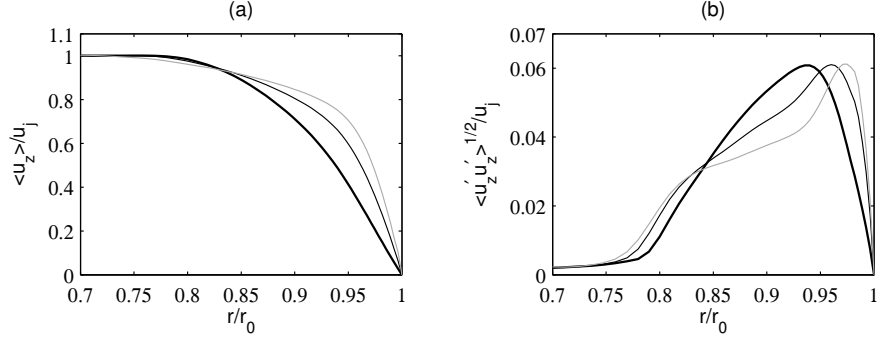


FIGURE 2. Radial profiles at the nozzle exit at  $z = 0$  (a) of mean axial velocity  $\langle u_z \rangle$  and (b) of the rms values of axial velocity fluctuations  $u'_z$ : — jetBL, — jetT1, - - jetT2.

---

	H	$\delta_\theta/r_0$	$\delta_{99}/r_0$	$\delta_\omega/r_0$	$Re_\theta$	$u'_e/u_j$	$r_e/r_0$	$n_\theta$
JetBL	2.29	0.0299	0.210	0.118	747	6.08%	0.935	50
JetT1	1.96	0.0280	0.220	0.062	700	6.10%	0.960	51
JetT2	1.71	0.0274	0.241	0.043	685	6.12%	0.975	64

---

TABLE 5. Nozzle-exit parameters: shape factor H, momentum thickness  $\delta_\theta$ , 99% velocity thickness  $\delta_{99}$  and vorticity thickness  $\delta_\omega$  of the boundary-layer profile, Reynolds number  $Re_\theta = u_j \delta_\theta / \nu$ , value  $u'_e/u_j$  and radial position  $r_e$  of peak axial turbulence intensity, and peak azimuthal mode  $n_\theta$  at  $r = r_e$ .

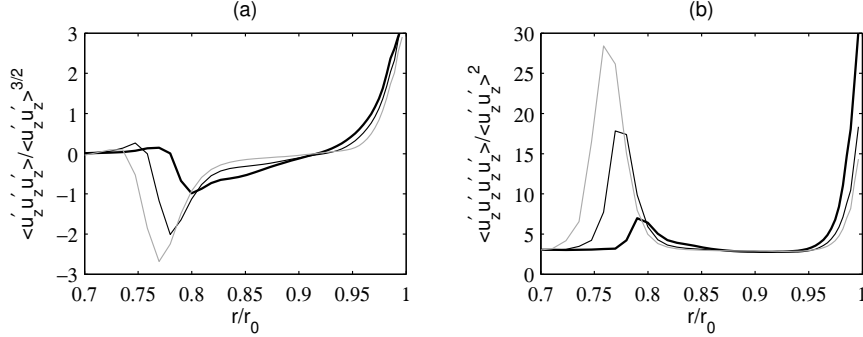


FIGURE 3. Radial profiles at the nozzle exit (a) of the skewness factor and (b) of the kurtosis factor of axial velocity fluctuations  $u'_z$ : — jetBL, — jetT1, - - jetT2.

451 obtained by Zaman (2017) who measured, also at  $r = r_0 - \delta_{94}$ , lower values of velocity  
 452 skewness for nominally laminar nozzle-exit conditions than for turbulent ones.

453 The properties of the jet initial disturbances are examined by computing spectra of  
 454 axial velocity fluctuations at the nozzle exit in both the inner and the outer boundary-  
 455 layer regions. The spectra estimated in the inner region at the position  $r = r_e$  of the  
 456 turbulence intensity peak, *i.e.* between  $r_e = 0.935r_0$  for jetBL and  $r_e = 0.975r_0$  for  
 457 jetT2, are represented as a function of the Strouhal number  $St_D$  in figure 4(a) and of  
 458 the azimuthal mode  $n_\theta$  in figure 4(b). Their shapes are roughly the same in the three  
 459 cases, and correspond, as was discussed in a specific note (Bogey *et al.* 2011c), to the  
 460 spectral shapes encountered for turbulent wall-bounded flows because of the presence  
 461 of large-scale elongated structures. As the boundary-layer profile changes from laminar

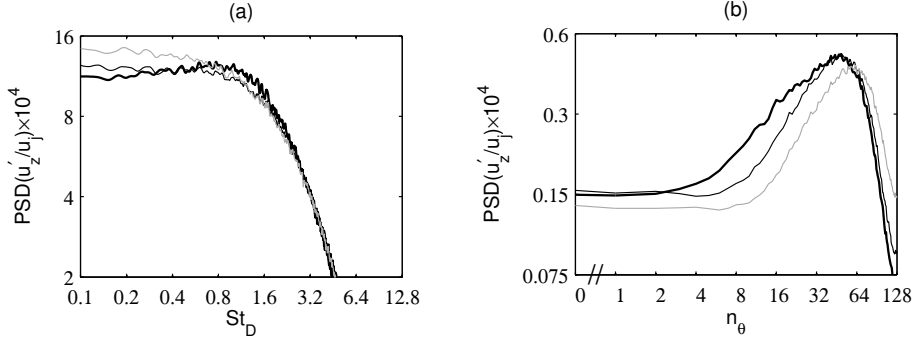


FIGURE 4. Power spectral densities (PSD) of axial velocity fluctuations  $u'_z$  obtained at the nozzle exit at the position  $r = r_e$  of peak axial turbulence intensity, as a function (a) of Strouhal number  $St_D$  and (b) of azimuthal mode  $n_\theta$ : — jetBL, - - jetT1, ··· jetT2.

462 to turbulent, the magnitude of the low-frequency components at  $St_D < 0.8$  slightly  
 463 strengthens in figure 4(a), which may be linked to the larger 99% velocity thickness of  
 464 the profile. Most obviously, the dominant components in figure 4(b) shift towards higher  
 465 modes, resulting in peaks at  $n_\theta = 50$  for jetBL,  $n_\theta = 51$  for jetT1 and  $n_\theta = 64$  for jetT2,  
 466 as reported in table 5. The turbulent structures are thus spaced out by  $\lambda_\theta = 0.13r_0$ ,  
 467  $\lambda_\theta = 0.12r_0$  and  $\lambda_\theta = 0.10r_0$ , respectively. The modification of their spatial arrangement  
 468 in the azimuthal direction may be related to the increase of the velocity gradient.

469 The spectra evaluated in the outer boundary-layer region at  $r = r_0 - \delta_{94} = 0.827r_0$   
 470 in all cases are depicted in figures 5. Their levels are normalized by the rms values of  
 471 velocity fluctuations at this position, equal to  $\langle u_z'^2 \rangle^{1/2} = 0.0248u_j$  for JetBL,  $0.0283u_j$   
 472 for JetT1 and  $0.0285u_j$  for JetT2. The spectra are very similar to each other, both in  
 473 shape and in amplitude. Compared to the near-wall spectra, two important differences  
 474 can be noticed. First, a significant amount of energy is contained by the components  
 475 centered around a Strouhal number of  $St_D = 3.2$  in figure 5(a), whereas a rapid collapse  
 476 is observed for  $St_D \geq 1.6$  in figure 4(a). Second, the dominant mode in the azimuthal  
 477 direction is  $n_\theta \simeq 40$  for all cases in figure 5(b), whereas it is higher, and increases for  
 478 a lower boundary-layer shape factor in figure 4(b). Therefore, the turbulent structures  
 479 organize differently near the wall and further away, as expected (Tomkins & Adrian  
 480 2005). Furthermore, they appear to depend on the form of the velocity profile in the first  
 481 region, but not in the second one.

### 482 3.1.2. Very near-nozzle instability waves

483 In order to characterize the instability waves initially growing in the shear layers, an  
 484 inviscid linear stability analysis is carried out following the methodology described in  
 485 section 2.4 from the LES mean flow profiles at  $z = 0.1r_0$ , corresponding to  $z \simeq 3.6\delta_\theta(0)$   
 486 in terms of nozzle-exit boundary-layer momentum thickness  $\delta_\theta(0)$ . The mean velocity  
 487 profiles at this position are shown in figure 6(a). They are very similar to the nozzle-exit  
 488 profiles of figure 2(a), and have momentum thicknesses only 2% larger than the exit values  
 489 reported in table 5. This persistence of the mean velocity profile is in agreement with  
 490 the measurements of Morris & Foss (2003) downstream of a sharp corner for a turbulent  
 491 boundary layer at  $Re_\theta = 4650$ , as indicated in table 1. For the comparison, a hyperbolic-  
 492 tangent velocity profile with  $\delta_\theta = 0.0288r_0$ , that is the momentum thickness imposed at  
 493 the pipe-nozzle inlet, is also plotted. This type of analytical profile is often used in linear  
 494 stability analyses for mixing layers and jets (Michalke 1984), providing good predictions  
 495 of the peak Strouhal number  $St_\theta$  for initially laminar conditions (Gutmark & Ho 1983),

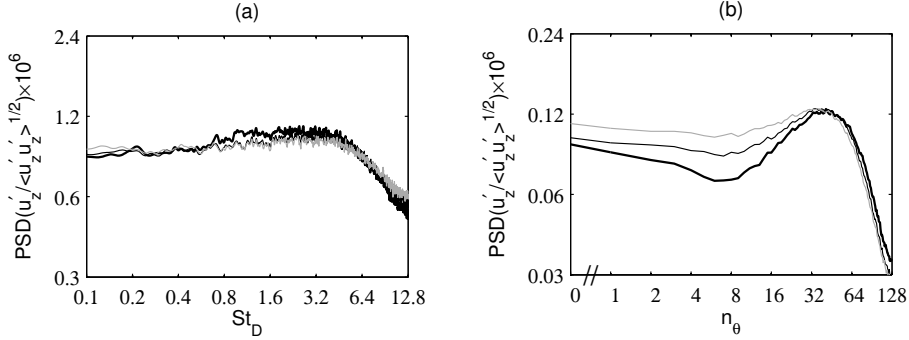


FIGURE 5. Power spectral densities of axial velocity fluctuations  $u'_z$  obtained at the nozzle exit at  $r = r_0 - \delta_{94}$ , as a function (a) of Strouhal number  $St_D$  and (b) of azimuthal mode  $n_\theta$ : — jetBL, - - - jetT1, ···· jetT2.

496 but poor ones for initially turbulent conditions (Drubka & Nagib 1981; Hussain & Zaman  
497 1985).

498 The instability amplification rates  $-\text{Im}(k_z)\delta_\theta$  computed for the first two azimuthal  
499 modes  $n_\theta = 0$  and  $n_\theta = 1$  are represented in figure 6(b) as a function of the Strouhal  
500 number  $St_\theta$ . Their peak frequencies are gathered in table 6. The curves obtained for the  
501 two modes are superimposed, due to the value of  $\delta_\theta/r_0 < 1/25$  (Michalke 1984), with a  
502 slight predominance of the axisymmetric mode. Their sensitivity to the velocity profile is  
503 much more spectacular. For jetBL, the range of unstable frequencies is narrower and the  
504 peak growth rate is higher than those for the hyperbolic-tangent profile. Despite these  
505 discrepancies, the peak growth rates are reached at very similar Strouhal numbers, namely  
506  $St_\theta = 0.018$  for jetBL and  $St_\theta = 0.017$  for the analytical profile. For the two other jets,  
507 the range of unstable frequencies broaden and the growth rates strengthen as the exit  
508 profile deviates from a laminar profile. In addition, the peak Strouhal number increases  
509 to  $St_\theta = 0.026$  for jetT1 and to  $St_\theta = 0.032$  for jetT2.

510 The present changes in peak frequency at  $z = 0.1r_0 \simeq 3.6\delta_\theta(0)$  depending on the  
511 boundary-layer profile are consistent with the data of the literature. For instance, the  
512 peak Strouhal numbers of  $St_\theta = 0.022 - 0.028$  measured by Drubka & Nagib (1981)  
513 and Hussain & Zaman (1985) in initially turbulent mixing layers are greater than those  
514 found around  $St_\theta = 0.013$  in initially laminar mixing layers. Closer to this study, in the  
515 experiments of Morris & Foss (2003), a hump emerges at  $St_\theta \simeq 0.06$  in the velocity  
516 spectrum acquired  $3.54\delta_\theta(0)$  downstream of a sharp edge, where  $\delta_\theta(0)$  here denotes the  
517 boundary-layer momentum thickness at the edge. Finally, the linear stability analyses  
518 performed at  $z = 0.08r_0$  in Fontaine *et al.* (2015) and at  $z = 0.16r_0$  in Brès *et al.* (2018)  
519 for the jets reported in table 1 also reveal peak amplification rates at higher  $St_\theta$  for  
520 turbulent than for laminar nozzle-exit flow conditions. Indeed, while the peak Strouhal  
521 numbers emerge at  $St_\theta = 0.012 - 0.014$  for the short-nozzle case in Fontaine *et al.* (2015)  
522 and for Baseline\_LES\_10M in Brès *et al.* (2018), they are equal to  $St_\theta = 0.09$  for the  
523 long-nozzle case and to  $St_\theta = 0.024$  for BL16M\_WM\_Turb. Remark that the positions of  
524  $z = 0.08r_0$  for the long-nozzle case and of  $z = 0.16r_0$  for BL16M\_WM\_Turb correspond  
525 respectively to  $z = 1.9\delta_\theta(0)$  and to  $z = 11\delta_\theta(0)$ . The variations of the peak frequencies  
526 with the axial position will be discussed later in section 3.2.3.

527 Instead of the momentum thickness, the peak frequency of the instability growth rates  
528 can be related to other length scales of the velocity profiles, such as the vorticity thick-  
529 ness  $\delta_\omega$  or viscous wall units at the nozzle exit, as proposed by Morris & Foss (2003).

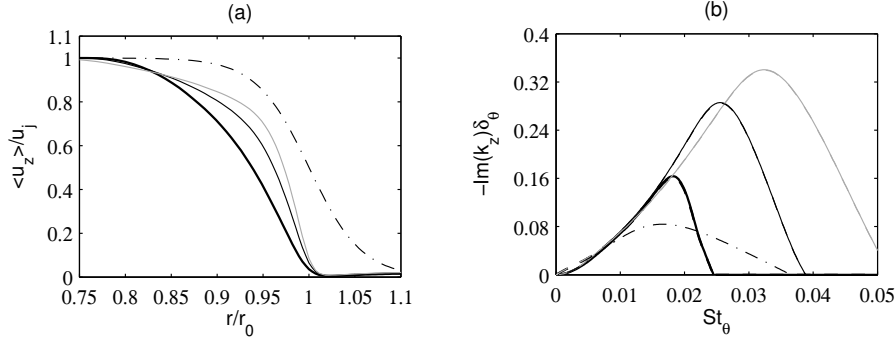


FIGURE 6. Representation (a) of the profiles of mean axial velocity  $\langle u_z \rangle$  at  $z = 0.1r_0$  and (b) of the instability growth rates  $-\text{Im}(k_z)$  obtained for the profiles using an inviscid linear stability analysis for modes  $n_\theta = 0$  for — jetBL, — jetT1, — jetT2 and  $n_\theta = 1$  for - - - jetBL, - - - jetT1, - - - jetT2, as a function of  $St_\theta$ ; ··· results for a 2-D hyperbolic-tangent velocity profile with  $\delta_\theta = 0.0288r_0$ .

---

	$St_D$	$St_\theta$	$St_\omega$	$St^+$
jetBL	1.21	0.018	0.071	0.078
jetT1	1.79	0.026	0.070	0.050
jetT2	2.30	0.032	0.067	0.040

---

TABLE 6. Peak Strouhal numbers  $St_D$ ,  $St_\theta$ ,  $St_\omega$  and  $St^+$  of instability growth rates obtained using an inviscid linear stability analysis at  $z = 0.1r_0$ .

---

530 The resulting Strouhal numbers  $St_\omega = f\delta_\omega/u_j$  and  $St^+ = f\nu/u_\tau^2$  are given in table 6.  
 531 As the boundary-layer shape factor  $H$  decreases, the latter varies from 0.078 for jetBL  
 532 down to 0.040 for jetT2, whereas the former remains very close to 0.07. Therefore, the  
 533 frequency of the initial instability wave is primarily linked to the high-shear portion of  
 534 the velocity profiles, as was noted by Fontaine *et al.* (2015).

535 The spectra of radial velocity fluctuations calculated at  $r = r_0$  at  $z = 0.1r_0$ ,  $z = 0.2r_0$   
 536 and  $z = 0.4r_0$  are represented in figure 7 as a function of  $St_D$ . The peak diameter-based  
 537 Strouhal numbers obtained from the mean flow profiles at  $z = 0.1r_0$  using the linear  
 538 stability analysis, provided in table 6, are also indicated. For all jets, a hump appears  
 539 in the spectra, centered on a frequency moving slowly towards lower frequencies in the  
 540 downstream direction, as for the separating boundary layer of Morris & Foss (2003). The  
 541 peak frequencies are in very good agreement with the linear stability results, especially  
 542 in figure 7(b) for  $z = 0.2r_0$ . Moreover, the hump rapidly grows, at a rate which is lowest  
 543 for jetBL and highest for jetT2, as predicted by the instability amplification rates of  
 544 figure 6(b). Therefore, for the present initially disturbed jets, the flow development very  
 545 near the nozzle is driven by the instability waves examined in this section.

### 546 3.2. Shear-layer development

#### 547 3.2.1. Vorticity snapshots

548 Instantaneous fields of vorticity norm obtained down to  $z = 3.5r_0$  and to  $z = 12r_0$   
 549 are represented in figures 8(a,c,e) and 8(b,d,f), respectively. Very near the nozzle lip, in  
 550 figures 8(a,c,e), the levels of vorticity are higher for jetT2 than for the two other jets  
 551 due to the sharper boundary-layer profile. In that region, the turbulent structures are  
 552 elongated in the downstream direction, which is characteristic of wall bounded flows.



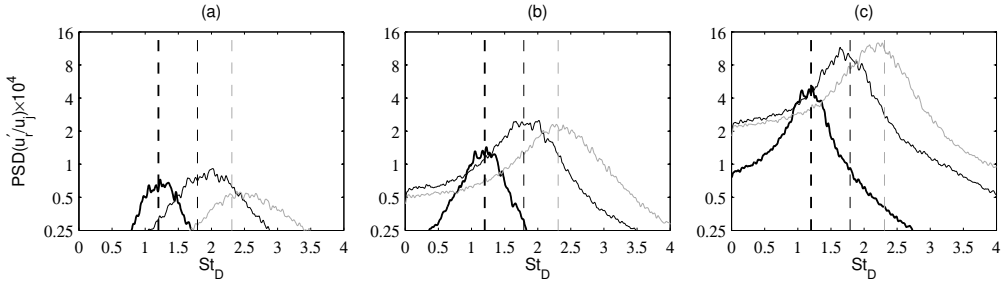


FIGURE 7. Power spectral densities of radial velocity fluctuations  $u'_r$  at  $r = r_0$  at (a)  $z = 0.1r_0$ , (b)  $z = 0.2r_0$  and (c)  $z = 0.4r_0$ , as a function of  $St_D$ : — jetBL, - - - jetT1, ··· jetT2; and peak frequencies of instability growth rates obtained using an inviscid linear stability analysis at  $z = 0.1r_0$ : - - - jetBL, - - - jetT1, - - - jetT2.

553 In the radial direction, their length scales are of the order of boundary-layer thickness  
 554 for jetBL, but are much smaller for jetT1 and especially for jetT2. For the latter jet, in  
 555 particular, strong levels of vorticity are only found around  $r = r_0$ . This is the case nearly  
 556 down to  $z = 0.5r_0$ , in agreement with the persistence of the mean boundary-layer profile  
 557 mentioned above. These results supports again that the initial shear-layer development is  
 558 essentially related to the vorticity thickness of the velocity profile. Further away from the  
 559 nozzle, the shear layers seem to roll up around  $z = 1.5r_0$  for jetBL but earlier for jetT1  
 560 and jetT2, which is in line with the instability amplification rates of the previous section.  
 561 Then, they exhibit typical features of turbulent mixing layers. Finally, in figures 8(b,d,f),  
 562 the mixing layers appear to be fully developed for  $z \gtrsim 4r_0$ . However, they spread faster  
 563 for jetBL than for the two other jets. The presence of large-scale structures resembling  
 564 the coherent structures of the flow visualizations of Brown & Roshko (1974) is also more  
 565 obvious for the laminar boundary-layer profile than for the non-laminar profiles. Similar  
 566 effects of the exit velocity profile on the organized structures in the shear layers of jets  
 567 were recently revealed by the experiments of Zaman (2017) using the ASME and the  
 568 conical nozzles. It should be reminded that the definition of coherent structures may  
 569 vary from one researcher to another. In this work, following Hussain (1986) and Fieldler  
 570 (1988), they refer to regions of correlated and concentrated vorticity, of size comparable  
 571 to the transverse length scale of the shear layer, which are spatially isolated from each  
 572 other and show similarity with the corresponding structures of the (preceding) laminar-  
 573 turbulent transition.

### 574 3.2.2. Flow field properties

575 The variations of the shear-layer momentum thickness are represented over  $0 \leq z \leq 6r_0$   
 576 in figure 9(a) and over  $0 \leq z \leq 15r_0$  in figure 9(b). The spreading rates  $d\delta_\theta/dz$  are  
 577 also shown in figure 9(a). The differences are significant between jetBL and jetT1 with  
 578 boundary-layer profiles with  $H = 2.29$  and  $H = 1.96$ , but they are rather weak between  
 579 the two transitional cases with  $H = 1.96$  and  $H = 1.71$ . For  $z \leq 3r_0$ , the mixing layers  
 580 develop faster for jetT1 and jetT2 than for jetBL. This can be due to the higher growth  
 581 rates of the jet initial instability waves as the shape factor  $H$  decreases, highlighted in  
 582 figure 6. Farther downstream, in contrast, the mixing layers spread most rapidly for  
 583 jetBL, which was suggested by the vorticity fields of figure 8, but has no evident cause at  
 584 first sight. In this region, a better agreement with the measurements of Fleury (2006) and  
 585 Castelain (2006) for jets at  $M = 0.9$  and  $Re_D \simeq 10^6$ , undoubtedly initially turbulent, is  
 586 obtained for the jets with non-laminar boundary-layer profiles. Furthermore, for jetBL,  
 587 the shear-layer spreading rate increases monotonically with the axial distance up to values

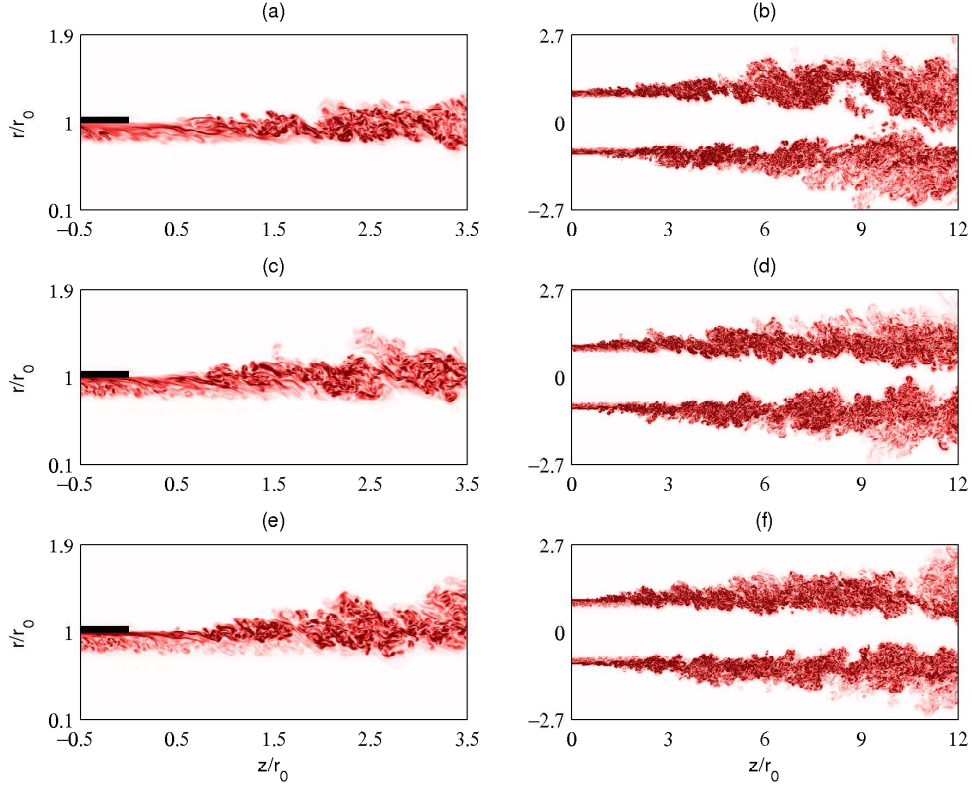


FIGURE 8. (Colour available at [journals.cambridge.org/flm](http://journals.cambridge.org/flm)) Snapshots in the  $(z, r)$  plane of vorticity norm  $|\omega|$  for (a) jetBL, (b) jetT1 and (c) jetT2. The color scales range from 0 up to (a,c,e)  $18u_j/r_0$  and (b,d,f)  $9u_j/r_0$ , from white to red.

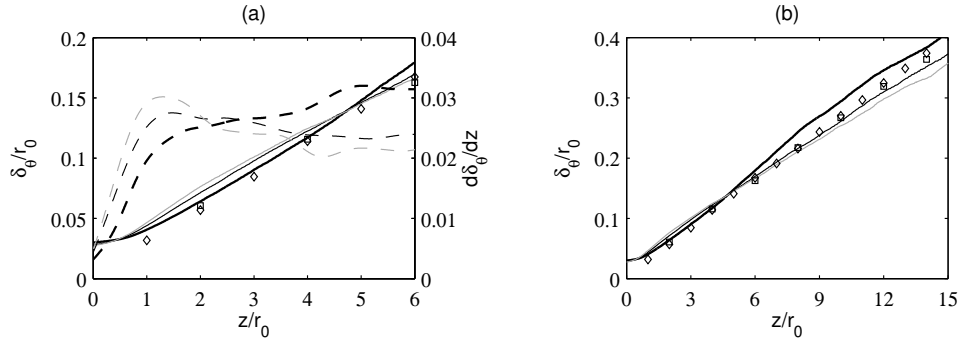


FIGURE 9. Variations of shear-layer momentum thickness  $\delta_\theta$  for — jetBL, — jetT1 and — jetT2 and of spreading rate  $d\delta_\theta/dz$  for - - - jetBL, - - - jetT1 and - - - jetT2; measurements for isothermal jets at  $M = 0.9$ :  $\diamond$  Fleury (2006) at  $Re_D = 7.7 \times 10^5$  and  $\square$  Castelain (2006) at  $Re_D = 10^6$ .

588 around 0.030 at  $z = 5r_0$ . For jetT1 and jetT2, on the contrary, they reach peak values  
 589 of 0.0275 at  $z = 1.3r_0$  and of 0.030 at  $z = 1.5r_0$ , respectively, and do not exceed values  
 590 of 0.024 for  $z \geq 4r_0$ .

591 In order to illustrate the change of the mean flow profiles in the region of boundary-  
 592 layer/mixing-layer transition, the profiles of mean axial velocity at  $z = 0.8r_0$ ,  $z = 1.6r_0$

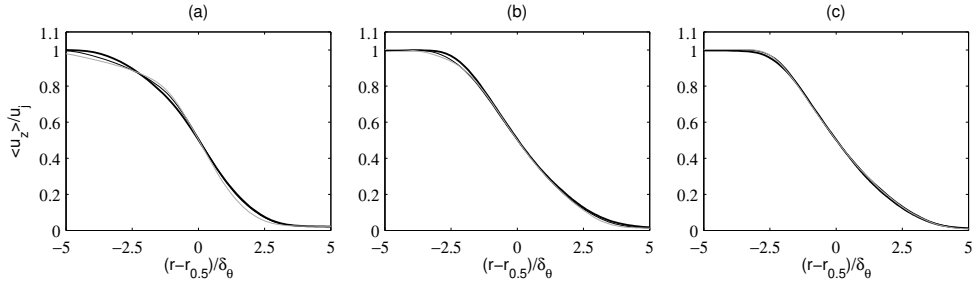


FIGURE 10. Radial profiles of mean axial velocity  $\langle u_z \rangle$  at (a)  $z = 0.8r_0$ , (b)  $z = 1.6r_0$  and (c)  $z = 3.2r_0$ : — jetBL, - - - jetT1, ···· jetT2.

593 and  $z = 3.2r_0$  are provided in figure 10. The radial distances are normalized by the local  
 594 shear-layer momentum thicknesses, which, however, are nearly the same in the present  
 595 jets at  $z = 0.8r_0$  and  $z = 3.2r_0$ , and only vary from  $0.054r_0$  in jetBL up to  $0.065r_0$  in  
 596 jetT2 at  $z = 1.6r_0$ . At  $z = 0.8r_0$ , corresponding to  $z = 28\delta_\theta(0)$ , the velocity profiles  
 597 differ significantly. This is particularly the case for their high-speed portions, which still  
 598 bear strong similarities with the nozzle-exit profiles. The latter result is consistent with  
 599 that obtained for a turbulent boundary layer at  $z = 29\delta_\theta(0)$  in the experiments of Morris  
 600 & Foss (2003). Farther away from the nozzle, the mean velocity profiles are very close  
 601 to each other at  $z = 1.6r_0$  and almost superimposed at  $z = 3.2r_0$ , and exhibit no clear  
 602 reminiscence of the boundary-layer profiles.

603 The rms values of axial and radial velocity fluctuations at  $r = r_0$  are displayed down to  
 604  $z = 15r_0$  in figure 11. They follow trends which are similar to those for the mixing-layer  
 605 spreading rate. Just downstream of the nozzle, they increase more rapidly for jetT1 and  
 606 jetT2 than for jetBL, thus reaching peaks around  $z = r_0$  in the former case, but  $z = 5r_0$   
 607 in the latter. In addition, the levels are lower for the transitional boundary-layer profiles.  
 608 This is true for the peak levels in the jets, given in table 7, which are equal, for  $u'_z$  and  
 609  $u'_r$  for instance, to approximately  $0.157u_j$  and  $0.12u_j$  for jetT1 and jetT2, but to  $0.174u_j$   
 610 and  $0.131u_j$  for jetBL. The difference in turbulence intensity is also significant down to  
 611  $z = 15r_0$ , which is roughly the position of the end of the jet potential core. Therefore,  
 612 the effects of the exit boundary-layer profile on the turbulence in the mixing layers last  
 613 far downstream of the nozzle, despite, notably, the nearly identical mean flow profiles  
 614 obtained at  $z = 3.2r_0$  in figure 10(c). Finally, as for the shear-layer momentum thickness,  
 615 the results for the jets with non-laminar mean velocity profiles better agree with the  
 616 measurements of Fleury (2006) and Castelain (2006) than those for jetBL.

617 Comparisons between numerical and experimental data may only be fully relevant for  
 618 identical upstream flow conditions. It can however be mentioned that in the similarity  
 619 region of an axisymmetric mixing layer, initially with  $\text{Re}_\theta = 349$ ,  $u'_e/u_j = 6.18\%$  and  
 620  $H = 2.47$ , Hussain & Zedan (1978b) obtained a spreading rate of 0.0294 and a peak axial  
 621 turbulence intensity of 16.7%, which are both comparable to the values reached in jetBL.  
 622 Moreover, the changes undergone by the mixing layers of the present jets as the nozzle-  
 623 exit velocity profile deviates from a laminar profile, namely a slower growth and weaker  
 624 velocity fluctuations, correspond to those observed experimentally when initially laminar  
 625 shear layers are tripped and become initially turbulent (Hill *et al.* 1976; Browand & Latigo  
 626 1979; Husain & Hussain 1979). They also resemble the changes induced by increasing  
 627 the exit turbulence levels only (Hussain & Zedan 1978a; Bogey *et al.* 2012b).

628 Finally, the skewness factors of the axial and radial velocity fluctuations at  $r = r_0$   
 629 are represented in figure 12. In the vicinity of the nozzle exit, in all cases, they differ

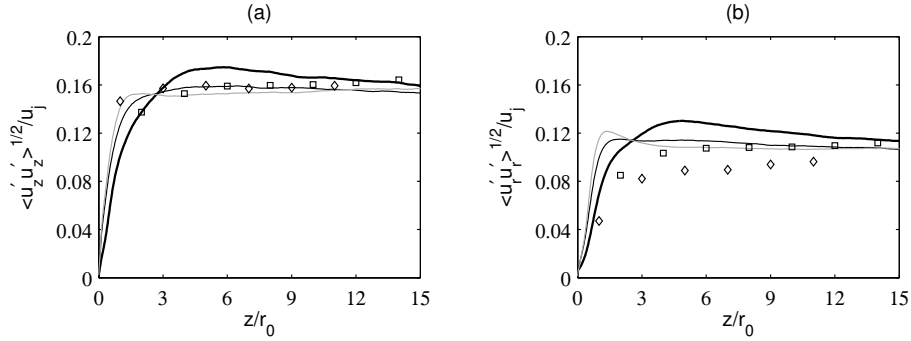


FIGURE 11. Variations of the rms values of (a) axial and (b) radial velocity fluctuations  $u'_z$  and  $u'_r$  at  $r = r_0$ : — jetBL, - - - jetT1, ··· jetT2; peak values measured in isothermal jets at  $M = 0.9$ :  $\diamond$  Fleury (2006) at  $Re_D = 7.7 \times 10^5$  and  $\square$  Castelain (2006) at  $Re_D = 10^6$ .

	$\langle u_z'^2 \rangle^{1/2} / u_j$	$\langle u_r'^2 \rangle^{1/2} / u_j$	$\langle u_\theta'^2 \rangle^{1/2} / u_j$	$\langle u'_r u'_z \rangle^{1/2} / u_j$
jetBL	17.4%	13.1%	14.5%	10.6%
jetT1	15.9%	11.7%	13.5%	9.6%
jetT2	15.5%	12.3%	14.0%	9.9%

TABLE 7. Peak turbulence intensities in the jets.

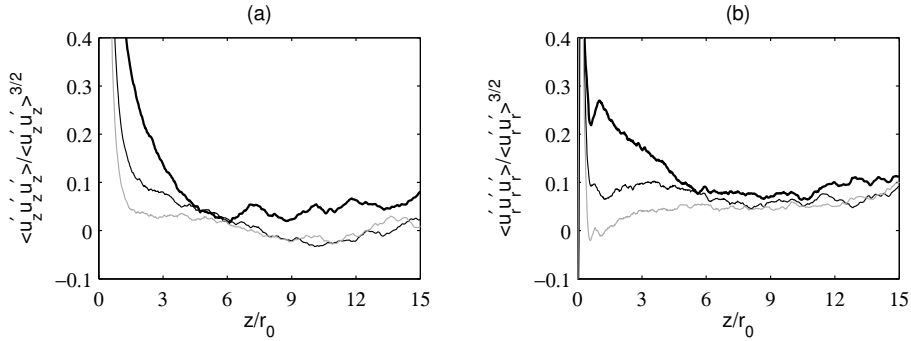


FIGURE 12. Variations of the skewness values of (a) axial and (b) radial velocity fluctuations  $u'_z$  and  $u'_r$  at  $r = r_0$ : — jetBL, - - - jetT1, ··· jetT2.

630 appreciably from zero, which is expected at the interface between the highly-disturbed  
 631 shear layers and the ambient medium. Their positive values are due to the sudden eruptions  
 632 of high-velocity fluid at the outer edge of the mixing layers. For jetT1 and jetT2,  
 633 the skewness factors rapidly decrease, whereas they remain greater than 0.1 down to  
 634  $z = 4r_0$  for jetBL. This can be related to the slower initial development of the shear  
 635 layers in the latter case. Farther downstream, for  $z \geq 6r_0$ , the skewness factors,  
 636 albeit much lower than previously, are still higher for jetBL than for the other jets. Given  
 637 the links between velocity skewness and large-scale vortices in free shear flows (Yule 1978),  
 638 this result suggests the presence of stronger coherent structures in the first jet.

### 639 3.2.3. Instability waves and velocity spectra

640 Some results of the inviscid linear stability analysis carried out, as reported in sec-  
 641 tion 2.4, from the LES mean flow fields between  $z = 0.02r_0$  and  $z = 5r_0$  are provided in

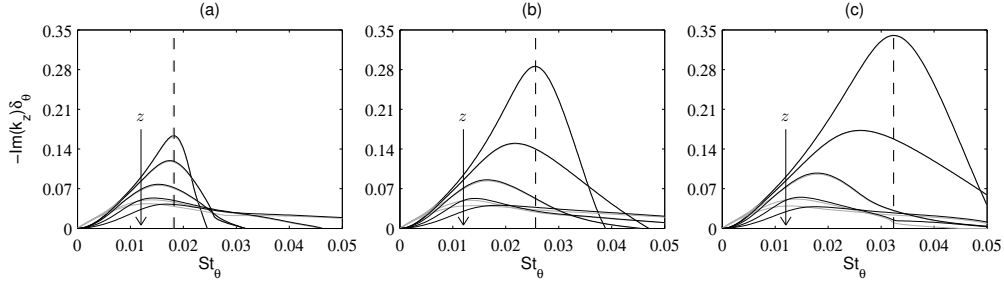


FIGURE 13. Representation of the instability growth rates  $-\text{Im}(k_z)\delta_\theta$  obtained using an inviscid linear stability analysis at  $z = 0.1r_0, 0.4r_0, 0.8r_0, 1.6r_0$  and  $3.2r_0$  for  $n_\theta = 0$  and  $n_\theta = 1$  for (a) jetBL, (b) jetT1 and (c) jetT2, as a function of  $St_\theta$ ;  $---$  peak frequencies at  $z = 0.1r_0$ .

642 order to investigate the properties of the instability waves, and their variations in the axial direction, during the boundary-layer/mixing-layer transition and further downstream,  
 643 They will help us to identify the possible cause of the differences between the shear-layer  
 644 developments.

645  
 646 The instability amplification rates  $-\text{Im}(k_z)\delta_\theta$  calculated for  $n_\theta = 0$  and  $n_\theta = 1$  at  $z =$   
 647  $0.1r_0, 0.4r_0, 0.8r_0, 1.6r_0$  and  $3.2r_0$  are represented in figure 13 as a function of the Strouhal  
 648 number  $St_\theta$ . The curves obtained for the two azimuthal modes are nearly superimposed  
 649 on each other except for  $z = 3.2r_0$ , where lower unstable frequencies are found for  
 650  $n_\theta = 1$  than for  $n_\theta = 0$  due to the mixing-layer thicknesses of  $\delta_\theta \simeq 0.1r_0$  at this location  
 651 (Michalke 1984). As the distance from the nozzle exit increases, the amplification curves  
 652 change appreciably in level and shape for all jets. For jetBL, the instability growth rates  
 653 are lower, and the ranges of unstable frequencies broaden. However, the peak Strouhal  
 654 numbers, equal to  $St_\theta = 0.018$  at  $z = 0.1r_0$ , do not vary much with the axial position. For  
 655 jetT1 and jetT2 with non-laminar boundary-layer profiles, the changes with the distance  
 656 from the nozzle are more important. The reduction of the growth rates is stronger and,  
 657 above all, the peak Strouhal numbers  $St_\theta$ , of 0.026 for jetT1 and of 0.032 for jetT2 at  
 658  $z = 0.1r_0$ , decrease significantly. At  $z = 3.2r_0$ , finally, the amplification curves are the  
 659 nearly the same for the three jets, which is not surprising given the very similar velocity  
 660 profiles of figure 10(c).

661 In order to highlight their variations downstream of the nozzle, the peak Strouhal  
 662 numbers  $St_\theta$  of the instability growth rates are plotted in figure 14(a) between  $z = 0.02r_0$   
 663 and  $z = 3.5r_0$ . The values obtained for  $n_\theta = 0$  and  $n_\theta = 1$  are identical to each other  
 664 down to  $z \simeq r_0$ , and then gradually diverge due to the thickening of the mixing layer,  
 665 yielding  $St_\theta \simeq 0.018$  for  $n_\theta = 0$  and  $St_\theta \simeq 0.014$  for  $n_\theta = 1$  at  $z = 3.5r_0$  in all cases. More  
 666 interestingly, strong discrepancies appear in the vicinity of the nozzle exit between the  
 667 three jets. In that region, for jetBL, the peak Strouhal numbers do not change much with  
 668 the axial distance and remain close to a value of  $St_\theta = 0.018$  corresponding roughly to  
 669 the Strouhal numbers emerging farther downstream in the mixing layers. For jetT1 and  
 670 jetT2, on the contrary, they rapidly decrease during the changeover from a boundary-  
 671 layer profile to a mixing-layer profile, from values of the order of or higher than 0.03 at  
 672  $z = 0.02r_0$  down to values lower than 0.02 at  $z \simeq 0.6r_0 \simeq 20\delta_\theta(0)$ . These variations of  
 673  $St_\theta$  are in very good agreement with the experimental data of Morris & Foss (2003) for  
 674 a turbulent boundary layer.

675 As in the study mentioned above, a scaling with the local shear-layer vorticity thickness  
 676 is applied to the peak frequencies of the instability growth rates. The resulting Strouhal  
 677 numbers  $St_\omega$  are shown in figure 14(b) between  $z = 0.02r_0$  and  $z = 3.5r_0$ . For the

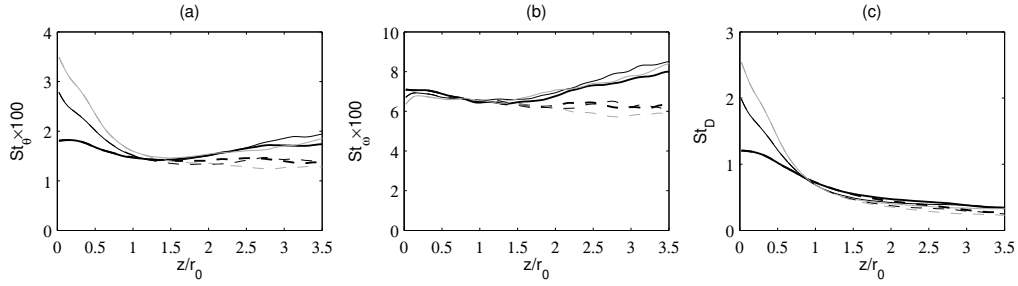


FIGURE 14. Axial variations of the peak Strouhal numbers (a)  $St_\theta$ , (b)  $St_\omega$  and (c)  $St_D$  of instability growth rates obtained for — jetBL, — jetT1, — jetT2 for  $n_\theta = 0$ ; - - -, - - -, - - - corresponding results for  $n_\theta = 1$ .

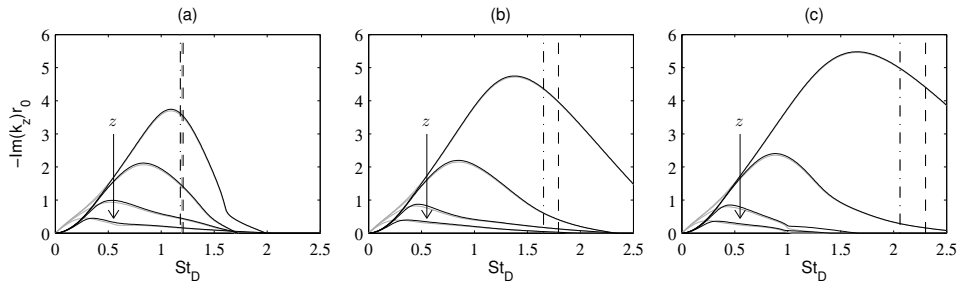


FIGURE 15. Representation of — the instability growth rates  $-\text{Im}(k_z)$  at  $z = 0.4r_0, 0.8r_0, 1.6r_0$  and  $3.2r_0$  as a function of  $St_D$  and of the peak frequencies at - - -  $z = 0.1r_0$  and - · -  $z = 0.2r_0$  obtained using an inviscid linear stability analysis for  $n_\theta = 0$  for (a) jetBL, (b) jetT1 and (c) jetT2; —, - - - and - · - - corresponding results for  $n_\theta = 1$ .

678 present jets, they are very close to each other at any of the locations considered. This  
 679 is particularly true, despite the different boundary-layer profiles, near the nozzle, where  
 680 Strouhal numbers  $St_\omega \simeq 0.07$  are continuously found between  $z = 0.02r_0$  and  $z \simeq 2r_0$ .  
 681 Therefore, for a given mean flow profile, the peak frequency of the instability waves is  
 682 only fixed by the maximum velocity gradient.

683 The variations of the most unstable Strouhal numbers  $St_\theta$  downstream of the nozzle  
 684 do not reflect those of the most unstable frequencies because of the increase of the shear-  
 685 layer momentum thickness in the axial direction. For that reason, the instability growth  
 686 rates  $-\text{Im}(k_z)r_0$  obtained for  $n_\theta = 0$  and  $n_\theta = 1$  at  $z = 0.4r_0, 0.8r_0, 1.6r_0$  and  $3.2r_0$   
 687 are re-plotted in figure 15 as a function of the diameter-based Strouhal number  $St_D$ . The  
 688 peak Strouhal numbers  $St_D$  are also represented in figure 14(c) between  $z = 0.02r_0$   
 689 and  $z = 3.5r_0$ . As the distance from the nozzle increases, they move to lower values due to the  
 690 shear-layer thickening. During the initial stage of flow development between the nozzle  
 691 exit and  $z \simeq 0.6r_0$ , the frequency decrease is however much more pronounced for jetT1  
 692 and jetT2 than for jetBL. In their linear stability analyses, Brès *et al.* (2018) recently  
 693 noted, as in this work, that downstream of the nozzle the range of the unstable frequencies  
 694 are more quickly reduced for their initially turbulent jet than for their initially laminar  
 695 jet with thicker exit boundary layer. They attributed this to the fact that the instability  
 696 waves in the near-nozzle region grow at a higher rate in the first jet because of the faster  
 697 shear-layer spreading in this case. On the basis of the present results, this appears to be  
 698 also strongly linked to the difference in peak instability frequency between laminar and  
 699 non-laminar boundary-layer profiles.

700 The dependence of the range of the unstable frequencies on the boundary-layer profiles

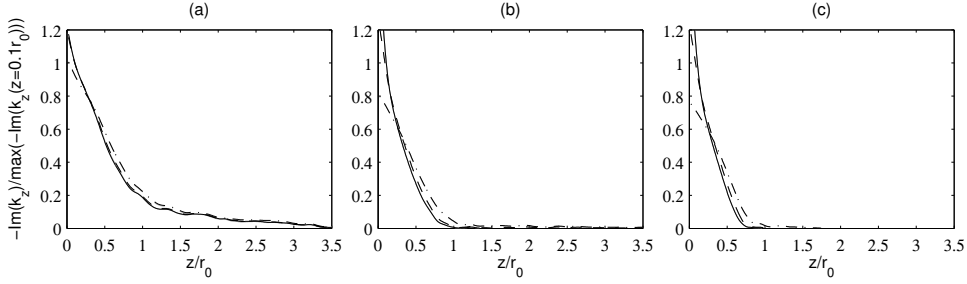


FIGURE 16. Axial variations of the instability growth rates obtained at the peak Strouhal numbers  $St_D$  at  $\text{---}$   $z = 0.1r_0$ ,  $\text{- - -}$   $z = 0.2r_0$  and  $\text{- \cdot - \cdot -}$   $z = 0.4r_0$  for  $n_\theta = 0$  for (a) jetBL, (b) jetT1 and (c) jetT2, normalized by the maximum growth rates at  $z = 0.1r_0$ ;  $\text{---}$ ,  $\text{- - -}$  and  $\text{- \cdot - \cdot -}$  corresponding results for  $n_\theta = 1$ .

701 has substantial effects on the spatial evolution of the instability waves developing down-  
 702 stream of the nozzle. Examine, for instance, the peak frequencies obtained at  $z = 0.1r_0$   
 703 in figure 15. The more non-laminar the boundary-layer profile, the earlier they leave the  
 704 range of the unstable frequencies. The growth rates calculated between  $z = 0.02r_0$  and  
 705  $z = 3.5r_0$  for the peak frequencies at  $z = 0.1r_0$ ,  $0.2r_0$  and  $0.4r_0$ , chosen to cover the  
 706 frequency range of the initial instability waves, are also represented in figure 16. In all  
 707 cases, they sharply decrease downstream of the nozzle. However, they remain appreciable  
 708 down to  $z \simeq 3.5r_0 \simeq 125\delta_\theta(0)$  in figure 16(a) for jetBL, whereas they become negligible  
 709 or negative as early as  $z \simeq r_0 \simeq 35\delta_\theta(0)$  in figures 16(b,c) for jetT1 and jetT2. As a  
 710 result, the instability waves developing very near the nozzle continue to be amplified,  
 711 even at a low rate, over a relatively large axial distance for the laminar boundary-layer  
 712 profile, whereas they are rapidly damped for the non-laminar profiles.

713 Velocity spectra computed in the mixing layers are discussed in light of the results of  
 714 the linear stability analysis. First, the spectra of radial velocity fluctuations obtained at  
 715  $r = r_0$  at  $z = 0.8r_0$ ,  $1.6r_0$ ,  $3.2r_0$ ,  $4.8r_0$ ,  $6.4r_0$  and  $10r_0$  are represented in figure 17 as  
 716 a function of the Strouhal number  $St_D$ , along with the peak frequencies of instability  
 717 growth rates at  $z = 0.1r_0$ . At  $z = 0.8r_0$ , in figure 17(a), the spectra resemble those of  
 718 figure 7 acquired farther upstream. They are dominated by humps associated with the  
 719 initial instability waves, peaking at frequencies slightly lower than those predicted at  
 720  $z = 0.1r_0$  due to the shear-layer thickening. As the distance from the nozzle increases, in  
 721 all cases, the humps diminish and eventually vanish as turbulence develops in the mixing  
 722 layers. However, for jetBL, the hump remains noticeable at  $z = 4.8r_0$  in figure 17(d),  
 723 whereas they cannot be observed at  $z = 3.2r_0$  in figure 17(c) for jetT1 and jetT2.  
 724 This discrepancy can be explained by the linear stability analysis, indicating a longer  
 725 persistence of the initial instability waves for the laminar boundary layer than for the  
 726 transitional ones. Farther downstream, at  $z = 6.4r_0$  and  $z = 10r_0$  in figures 17(e,f), the  
 727 spectra are all broadband, but significant differences appear at low frequencies. More  
 728 precisely, the levels are higher for jetBL than for jetT1 and jetT2 at  $St_D \lesssim 1$ . Therefore,  
 729 in the jet with a laminar boundary layer, the initial instability components last over a  
 730 larger distance, but also lead to stronger large-scale structures in the mixing layers after  
 731 having disappeared. These results are in line with the comments on coherent structures  
 732 made previously from the vorticity fields and the skewness factors at  $r = r_0$ , and with  
 733 the visualizations of Zaman (2017) for initially nominally laminar jets.

734 In order to explore the azimuthal distribution of the flow disturbances, the spectra  
 735 of radial velocity fluctuations at  $r = r_0$  at  $z = 0.8r_0$ ,  $3.2r_0$  and  $10r_0$  are depicted in  
 736 figure 18 as a function of mode  $n_\theta$ . At the first location, in figure 18(a), the spectra have

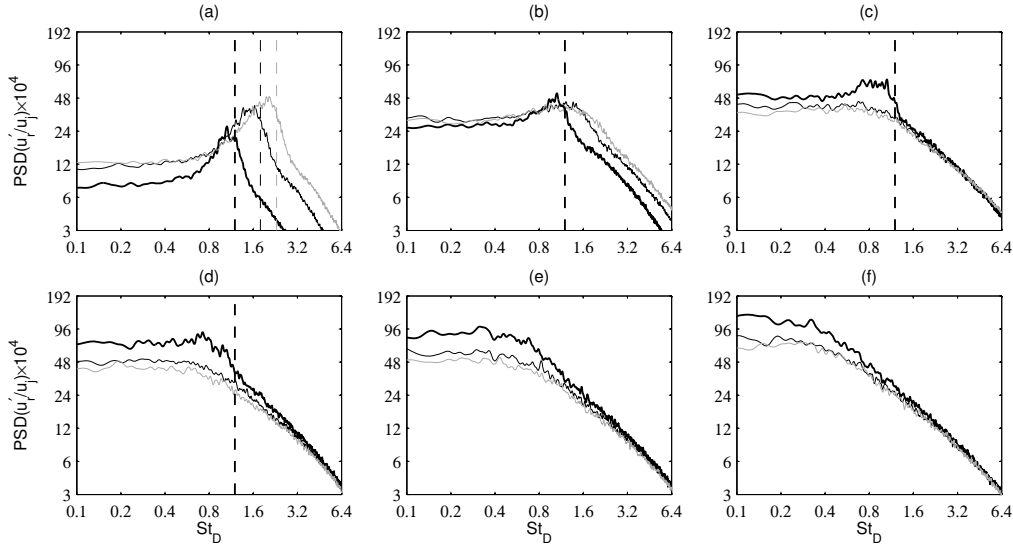


FIGURE 17. Power spectral densities of radial velocity fluctuations  $u'_r$  at  $r = r_0$  at (a)  $z = 0.8r_0$ , (b)  $z = 1.6r_0$ , (c)  $z = 3.2r_0$ , (d)  $z = 4.8r_0$ , (e)  $z = 6.4r_0$  and (f)  $z = 10r_0$  as a function of  $St_D$ : — jetBL, — jetT1, — jetT2; peak frequencies of instability growth rates obtained using an inviscid linear stability analysis at  $z = 0.1r_0$ : - - - jetBL, - - - jetT1, - - - jetT2.

737 nearly identical shapes over the whole range of modes considered. Since the azimuthal  
 738 velocity spectra at the nozzle exit are also close to each other in figures 4(b) and 5(b),  
 739 the mechanisms at play between  $z = 0$  and  $z = 0.8r_0$  are of the same nature in the three  
 740 jets. The levels are highest for jetT2 and lowest for jetBL, and for a given jet, they are  
 741 maximum for the axisymmetric mode, remain strong up to modes  $n_\theta = 3$  or 4, and then  
 742 sharply decrease for higher modes. These trends are consistent with the features of the  
 743 instability waves initially growing in the shear layers, namely higher amplification rates  
 744 for a more turbulent nozzle-exit boundary layer, and very similar rates for the first five  
 745 azimuthal modes (Brès *et al.* 2018). Farther downstream, at  $z = 3.2r_0$  and  $z = 10r_0$  in  
 746 figure 18(b,c), the spectra are superimposed for  $n_\theta \geq 16$ , but the levels are higher for  
 747 jetBL than for jetT1 and jetT2 at lower mode numbers. The difference in level is largest  
 748 for  $n_\theta \leq 2$  at  $z = 3.2r_0$ , which may be related to the presence of instability components  
 749 at this position for jetBL, and for  $n_\theta \leq 5$  at  $z = 10r_0$ . The intense large-scale structures  
 750 in the mixing layers of jetBL revealed by the spectra of figures 17(c-f) are consequently  
 751 significantly correlated in the azimuthal direction.

752 Finally, the spectra of radial velocity fluctuations at  $r = r_0$  at  $z = 0.8r_0$ ,  $3.2r_0$  and  
 753  $10r_0$  for mode  $n_\theta = 1$  are displayed in figure 19 as a function of  $St_D$ . For brevity, only the  
 754 results for  $n_\theta = 1$  are reported, but those obtained for the other first azimuthal modes are  
 755 very similar. As in figures 17(a,c,f), humps associated with the initial instability waves  
 756 dominate at  $z = 0.8r_0$ , the hump still appears only for jetBL at  $z = 3.2r_0$ , and the  
 757 low-frequency components are stronger for jetBL than for the other jets at  $z = 10r_0$ . The  
 758 instability waves however emerge more clearly in the present case than in the spectra  
 759 computed from the full velocity fields. Compared to the broadband levels, indeed, their  
 760 peak levels are more than two decades higher in figure 19(a), whereas they are 3-4 times  
 761 higher in figure 17(a).



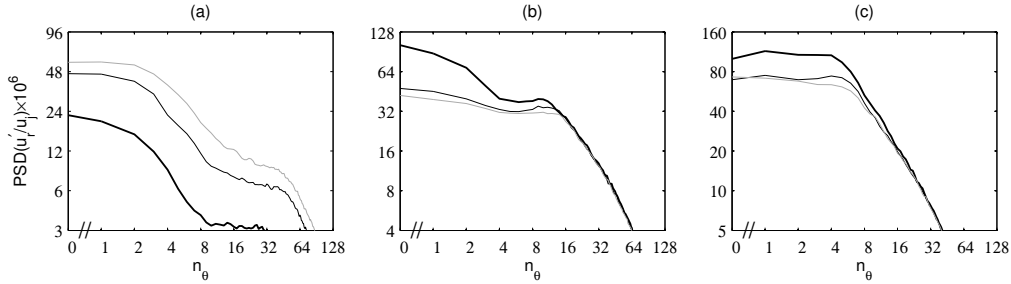


FIGURE 18. Power spectral densities of radial velocity fluctuations  $u'_r$  at  $r = r_0$  (a)  $z = 0.8r_0$ , (b)  $z = 3.2r_0$  and (c)  $z = 10r_0$ , as a function of mode  $n_\theta$ : — jetBL, - - - jetT1, ··· jetT2.

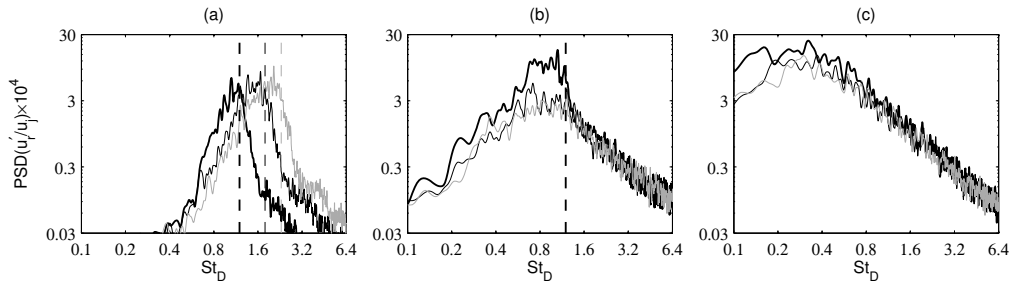


FIGURE 19. Power spectral densities for mode  $n_\theta = 1$  of radial velocity fluctuations  $u'_r$  at  $r = r_0$  at (a)  $z = 0.8r_0$ , (b)  $z = 3.2r_0$  and (c)  $z = 10r_0$ , as a function of  $St_D$ : — jetBL, - - - jetT1, ··· jetT2; peak frequencies of instability growth rates obtained using an inviscid linear stability analysis at  $z = 0.1r_0$ : - - - jetBL, - - - jetT1, - - - jetT2.

762

### 3.3. Jet development

#### 3.3.1. Vorticity snapshots

763 Snapshots of the vorticity norm obtained from the nozzle exit down to  $z = 25r_0$  are  
 764 provided in figure 20. Overall, they look like each other, and display, from upstream to  
 765 downstream, the growth of the turbulent mixing layers, the closing of the jet potential  
 766 cores and the regions of developed jet flows. Large-scale coherent structures may also  
 767 be seen in the shear layers, for instance at  $z \simeq 11r_0$  for jetBL and at  $z \simeq 12r_0$  for  
 768 jetT2. As the shape factor of the exit boundary-layer profile decreases, the mixing layers  
 769 visibly merge later, as expected given the reduction in shear-layer spreading rate noted  
 770 in previous section. As a result, the end of the potential core is located around  $z = 13r_0$   
 771 in figure 20(a) for the laminar boundary-layer profile, but around  $z = 15r_0$  in figure 20(c)  
 772 for the transitional profile with  $H = 1.71$ .  
 773

#### 3.3.2. Flow field properties

774 The variations of the centerline mean axial velocity are presented in figure 21. In  
 775 figure 21(a), as the nozzle-exit boundary-layer profile changes from laminar to turbulent,  
 776 the jet flow develops more slowly. The potential core thus ends at  $z_c = 12.4r_0$  for jetBL,  
 777  $14.8r_0$  for jetT1 and  $15.6r_0$  for jetT2, as indicated in table 8, where  $z_c$  is defined such  
 778 as  $\langle u_z \rangle(z_c) = 0.95u_j$  at  $r = 0$ . Even if the comparisons must be taken with care due  
 779 to the moderate Reynolds number and the thick initial shear layers of the present jets,  
 780 this leads to a better agreement with the measurements of Lau *et al.* (1979) and Fleury  
 781 *et al.* (2008) for jets at  $M = 0.9$  and  $Re_D \simeq 10^6$  plotted in the figure. Downstream of  
 782 the potential core, the centerline velocity seems to decay at a similar rate in three jets.  
 783

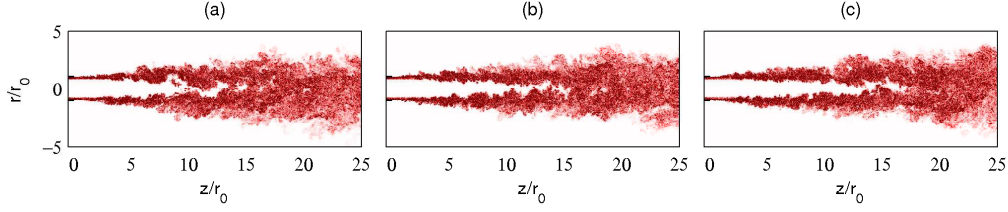


FIGURE 20. (Colour available at [journals.cambridge.org/flm](http://journals.cambridge.org/flm)) Snapshots in the  $(z, r)$  plane of vorticity norm  $|\omega|$  for (a) jetBL, (b) jetT1 and (c) jetT2. The color scale ranges from 0 up to  $5.5u_j/r_0$ , from white to red.

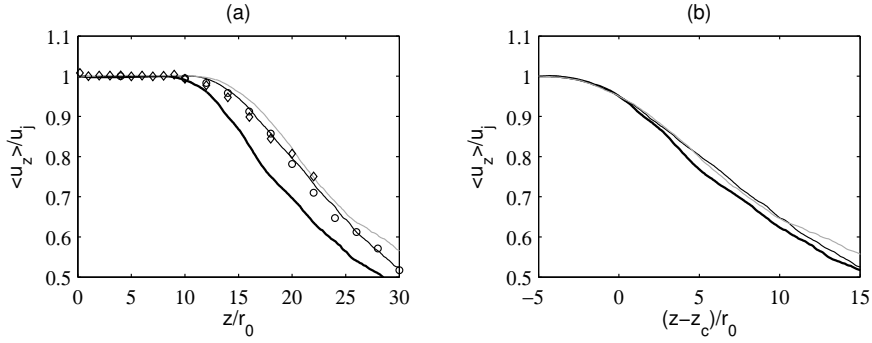


FIGURE 21. Variations of centerline mean axial velocity  $\langle u_z \rangle$  as a function of (a)  $z$  and (b)  $z - z_c$ : — jetBL, — jetT1, — jetT2; measurements for isothermal jets at  $M = 0.9$ :  $\circ$  Lau *et al.* (1979) at  $Re_D = 10^6$  and  $\diamond$  Fleury *et al.* (2008) at  $Re_D = 7.7 \times 10^5$ .

	$z_c/r_0$	$\langle u_z'^2 \rangle^{1/2}/u_j$	$\langle u_r'^2 \rangle^{1/2}/u_j$
JetBL	12.4	14.3%	11%
JetT1	14.8	12.9%	10.1%
JetT2	15.6	13.7%	10.3%

TABLE 8. Axial position of the end of the potential core  $z_c$  and peak rms values of velocity fluctuations  $u'_z$  and  $u'_r$  on the jet axis.

784 According to figure 21(b), however, the decay rate is slightly lower for jetT1 and jetT2  
785 than for jetBL.

786 The centerline rms values of axial velocity fluctuations are shown in figure 22(a). As  
787 for the mean flow profiles, the differences are significant between jetBL and the two jets  
788 with transitional boundary-layer profiles, but relatively weak between the latter jets.  
789 The results are also closer to the experimental data of Lau *et al.* (1979) and Fleury *et al.*  
790 (2008) for jetBL. The peak turbulence intensities are reached at  $z \simeq 17r_0$  for jetBL but  
791 later at  $z \simeq 22r_0$  for the two other jets, which corresponds, relative to the end of the  
792 potential core, to  $z \simeq z_c + 5r_0$  and  $z_c + 7r_0$  respectively. They are equal to 14.3% for  
793 jetBL, but decrease approximately down to 13% for the jets with non-laminar boundary-  
794 layer profiles, see also in table 8 for the radial turbulence intensities. This trend is similar  
795 to that obtained in the mixing layers down to  $z = 15r_0$  in figure 11.

796 The spectra of the centerline axial velocity fluctuations at  $z = z_c + 5r_0$ , *i.e.* roughly  
797 at the positions of the peak rms levels, are depicted in figure 22(b) as a function of  
798  $St_D$ . The spectra are superimposed and follow a  $-5/3$  power law at  $St_D \geq 0.5$ , but

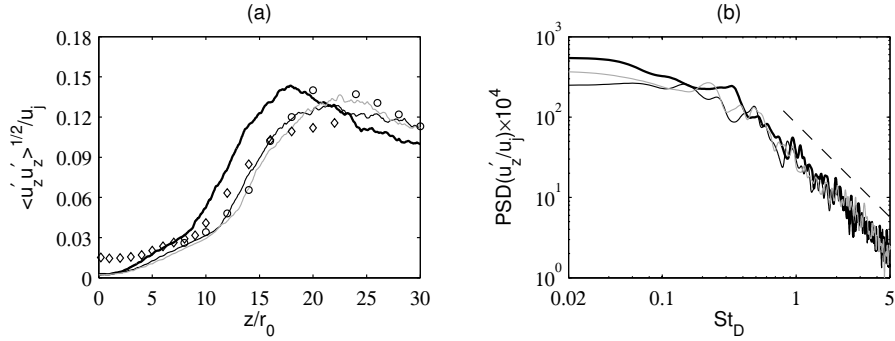


FIGURE 22. Properties of the centerline axial velocity fluctuations  $u'_z$ : (a) axial variations of rms values and (b) power spectral densities at  $z = z_c + 5r_0$  as a function of  $St_D$  for — jetBL, — jetT1, — jetT2; same symbol types as in figure 21; - - -  $St_D^{-5/3}$ .

799 they significantly differ and show highest levels for jetBL at lower Strouhal numbers.  
 800 Therefore, stronger large-scale structures are found not only in the mixing layers, but  
 801 also downstream of the potential core for the jet with a laminar boundary-layer profile.  
 802 This may be the cause for the divergence in velocity decay of figure 21(b).

803 The changes observed between the present jets with laminar and transitional exit mean  
 804 velocity profiles are comparable to those obtained experimentally between untripped and  
 805 tripped jets (Raman *et al.* 1989, 1994; Russ & Strykowski 1993), as well as to those  
 806 happening when the initial fluctuation level increases (Bogey *et al.* 2012*b*). In particular,  
 807 in Raman *et al.* (1989), tripped and untripped jets at  $M = 0.3$  and  $Re_D = 6 \times 10^5$   
 808 with nozzle-exit turbulence intensities  $u'_e/u_j \simeq 7\%$  and boundary-layer shape factors  
 809  $H \simeq 1.55$  and  $1.80$ , respectively, were considered. The flow development in the tripped  
 810 jets is shifted by  $2r_0$  in the downstream direction with respect to the untripped jet, which  
 811 is in line with the results of this study. However, the peak turbulence intensities on the  
 812 centerline, located at  $z \simeq z_c + 7r_0$ , are similar in the tripped and untripped jets, which  
 813 disagrees with figure 22. The reason for this may be that the exit boundary layer of the  
 814 untripped jet of Raman *et al.* (1989) is not laminar but transitional. This may also be  
 815 due to the larger boundary-layer thickness in the simulations (Bogey & Marsden 2013).

### 816 3.4. Acoustic fields

#### 817 3.4.1. Pressure snapshots

818 Snapshots of the pressure fields obtained in the LES are given in figure 23. In all  
 819 cases, large-scale hydrodynamic fluctuations, classically attributed to the flow coherent  
 820 structures (Arndt *et al.* 1997), dominate within and very near the jets. Farther from  
 821 the axis, sound waves emerge and propagate in the acoustic field. The waves emitted in  
 822 the flow direction are strong and have long wavelengths, which is typical of the down-  
 823 stream subsonic jet noise component (Tam *et al.* 2008). Those travelling in the sideline  
 824 and upstream directions are weaker and have shorter wavelengths. For the three jets,  
 825 the latter ones appear to be mainly generated between  $z = 5r_0$  and  $z = 10r_0$ . Their  
 826 amplitudes, however, are visibly higher for jetBL in figure 23(a) than for jetT1 and jetT2  
 827 in figures 23(b,c).

#### 828 3.4.2. Near-field and far-field pressure levels

829 The properties of the jet acoustic near fields are investigated from the pressure signals  
 830 recorded at  $r = L_r = 15r_0$  during the LES. Those of the jet far fields are characterized

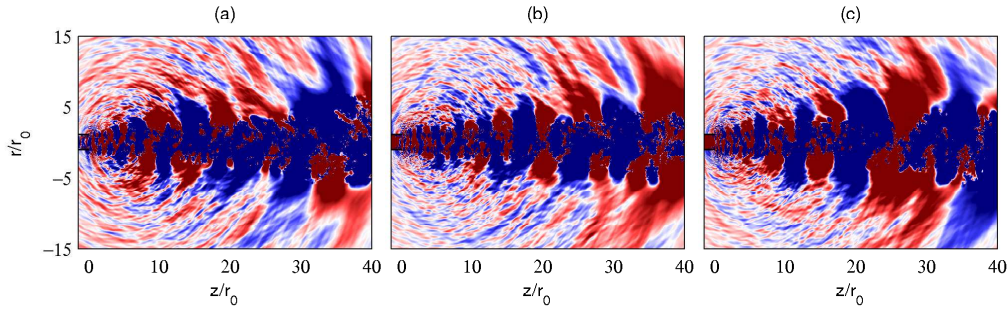


FIGURE 23. (Colour available at [journals.cambridge.org/flm](http://journals.cambridge.org/flm)) Snapshots in the  $(z, r)$  plane of pressure fluctuations  $p - p_a$  for (a) jetBL, (b) jetT1 and (c) jetT2. The color scale ranges from  $-70$  to  $70$  Pa, from blue to red.

831 from the fluctuations given at  $150$  radii from the nozzle exit by the two ILEE compu-  
 832 tations of sound propagation described in section 2.5. In the second case, the results  
 833 presented thereafter for the angles  $\phi \leq 60^\circ$  relative to the jet direction are obtained in  
 834 the computation in which the LES data are imposed onto the ILEE grid for  $r \geq 7.5r_0$   
 835 at  $z = L_z = 40r_0$  in order to capture most of the downstream noise components. Those  
 836 for  $\phi \geq 60^\circ$  come from the computation in which the LES/ILEE coupling at  $z = L_z$   
 837 is carried out only for  $r \geq 14r_0$  to avoid the generation of significant spurious waves for  
 838 large radiation angles where the noise levels are weak. It should be noted that the two  
 839 far-field extrapolations provide nearly identical results at  $\phi = 60^\circ$  for Strouhal numbers  
 840 greater than  $St_D = 0.075$ , demonstrating the negligible influence of the downstream ex-  
 841 trapolation surface on the frequencies of interest. The overall sound pressure levels in  
 842 this paper are all calculated by integrating the sound spectra from the Strouhal number  
 843 value given above.

844 The noise levels obtained at  $r = 15r_0$  between  $z = 0$  and  $40r_0$ , and at  $150$  radii from  
 845 the nozzle exit between  $\phi = 15^\circ$  and  $150^\circ$  are represented in figure 24. For illustration  
 846 purposes, the experimental data of Bogey *et al.* (2007) and Bridges & Brown (2005)  
 847 for isothermal jets at  $M = 0.9$  and  $Re_D \simeq 10^6$  are also plotted. With respect to the  
 848 simulated jets, these jets have 15-20 times higher Reynolds numbers and certainly quite  
 849 different nozzle-exit conditions, including much thinner exit boundary layers, which may  
 850 be the cause for the extra noise radiated by the jet of Bogey *et al.* (2007) in figure 24(a).  
 851 Despite this, however, a good qualitative agreement is found with the simulation results.  
 852 More importantly, for all near-field and far-field observation points, the noise levels are  
 853 2-3 dB higher for jetBL with a laminar boundary-layer profile than for the two jets with  
 854 transitional profiles. In addition, the levels for jetT2 are just very slightly lower than  
 855 those for jetT1. These trends are very similar to those reported for the rms values of  
 856 velocity fluctuations in the jets, as expected due to the links existing between acoustic  
 857 sources and turbulence intensities in subsonic jets (Zaman 1986).

858 The sound pressure levels obtained at  $r = 15r_0$  for the modes  $n_\theta = 0, 1$  and  $2$  are shown  
 859 in figure 25. The levels for  $n_\theta = 0$  are maximum at  $z = L_z = 40r_0$  and sharply decrease  
 860 in the upstream direction, whereas those for  $n_\theta = 1$  and  $2$  reach a peak at  $z \simeq 25r_0$   
 861 and  $z \simeq 20r_0$ , respectively. These peak positions are consistent with the the far-field  
 862 directivities found experimentally for the first azimuthal modes. For instance, for the jet  
 863 at  $M = 0.6$  of Cavalieri *et al.* (2012), noise is strongest in the downstream direction for  
 864 the axisymmetric mode and for the angles of  $\phi = 30^\circ$  for  $n_\theta = 1$  and of  $\phi = 40^\circ$  for  
 865  $n_\theta = 2$ . Here, for each mode considered, the noise levels are 2-3 dB higher for jetBL  
 866 than for jetT1 and jetT2, and the levels for the last two jets do not differ appreciably,

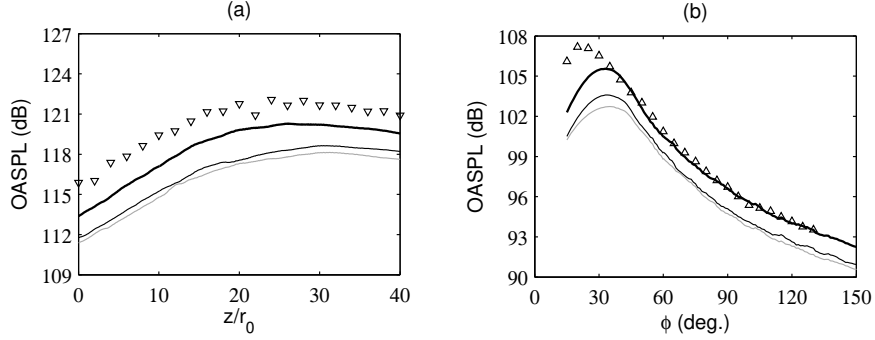


FIGURE 24. Overall sound pressure levels (OASPL) obtained (a) at  $r = 15r_0$  and (b) at a distance of  $150r_0$  from the nozzle exit as a function of the angle  $\phi$  relative to the jet direction: — jetBL, — jetT1, — jetT2; measurements for isothermal jets at  $M = 0.9$ :  $\nabla$  Bogey *et al.* (2007) at  $Re_D = 7.9 \times 10^5$  and  $\triangle$  Bridges & Brown (2005) at  $Re_D = 10^6$ .

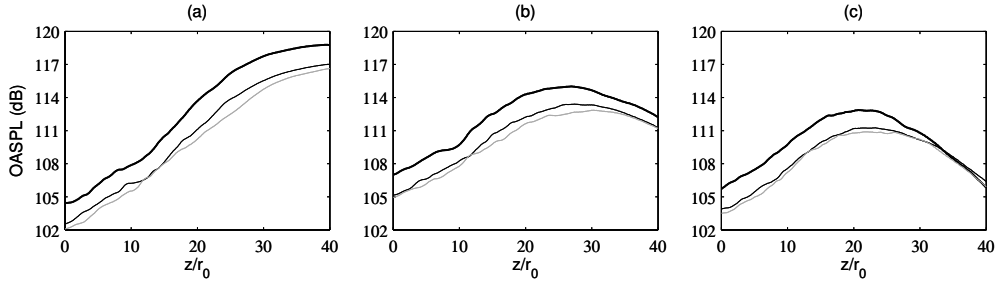


FIGURE 25. Overall sound pressure levels obtained at  $r = 15r_0$  for modes (a)  $n_\theta = 0$ , (b)  $n_\theta = 1$  and (c)  $n_\theta = 2$ : — jetBL, — jetT1, — jetT2.

867 just as in figure 24 for the full pressure signals. This is in line with the resemblances of  
 868 the features of the full velocity flow fields and of their first modal components in the  
 869 azimuthal direction, depicted in figures 17 and 19.

870 The pressure spectra calculated at  $r = 15r_0$  at  $z = 0, 20r_0$  and  $40r_0$  are represented  
 871 in figure 26 as a function of the Strouhal number  $St_D$ . Those evaluated in far field  
 872 for the angles of  $\phi = 30^\circ, 90^\circ$  and  $150^\circ$  are provided in figure 27. When possible, the  
 873 corresponding measurements of Bogey *et al.* (2007) and Bridges & Brown (2005) for jets  
 874 at  $Re_D \simeq 10^6$  are shown. As for the overall sound levels, they compare well with the  
 875 simulation results, with a better fit for the data of Bridges & Brown (2005). The spectra  
 876 for the present jets have similar shapes, typical of subsonic jet noise (Mollo-Christensen  
 877 *et al.* 1964; Tam 1998). For small radiation angles, in figure 26(c) and figure 27(a),  
 878 they are dominated by a narrow-band component centered around  $St_D = 0.2$ . The noise  
 879 levels are 2-3 dB higher for jetBL than for the two other jets for  $St_D \leq 0.3$ , but are  
 880 rather close to each other for  $St_D \geq 0.6$ . This can be related to the velocity spectra of  
 881 figures 17(f) and 22(b) obtained near the end of the potential core, where the downstream  
 882 acoustic components originate (Panda *et al.* 2005; Bogey & Bailly 2007; Tam *et al.*  
 883 2008; Bogey 2019), which also contain stronger low-frequency components for jetBL  
 884 but are superimposed at high frequencies. For large radiation angles, in figures 26(a,b)  
 885 and 27(b,c), the pressure spectra are broadband. In that case, the emitted sound is louder  
 886 for jetBL than for jetT1 and jetT2 not only at  $St_D \leq 0.3$  as previously, but also at higher  
 887 Strouhal numbers. In particular, an increase of 1-1.5 dB is noted over  $1.2 \leq St_D \leq 4.8$ .  
 888 This most likely results from the higher turbulence intensities in the mixing layers for

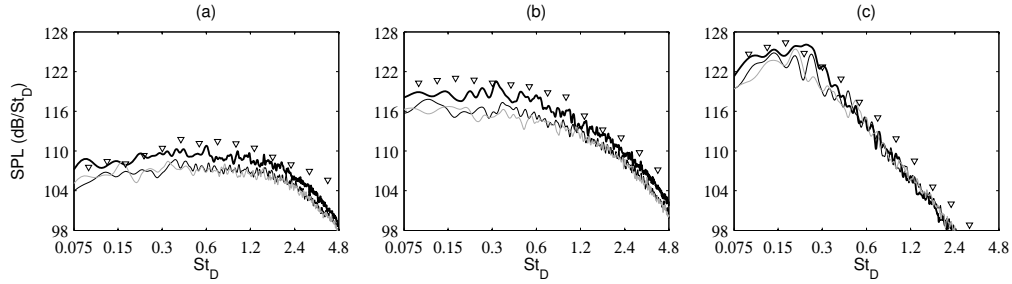


FIGURE 26. Sound pressure levels (SPL) obtained at  $r = 15r_0$  at (a)  $z = 0$ , (b)  $z = 20r_0$  and (c)  $z = 40r_0$ , as a function of  $St_D$ : — jetBL, - - - jetT1, ··· jetT2;  $\nabla$  measurements of Bogey *et al.* (2007) for an isothermal jet at  $M = 0.9$  and  $Re_D = 7.9 \times 10^5$ .

889 jetBL, in a region where the acoustic sources have a wide range of frequencies (Chu  
 890 & Kaplan 1976; Fisher *et al.* 1977; Narayanan *et al.* 2002; Lee & Bridges 2005). The  
 891 difference at  $St_D \geq 3.2$  is however rather surprising given the velocity spectra of figures 17  
 892 and 22, none of which exhibits stronger components at such high Strouhal numbers for  
 893 jetBL.

894 It is difficult to compare the present results with the experimental data available for  
 895 tripped and untripped jets, because tripping usually mainly results in removing the noise  
 896 generated by the vortex pairings occurring in fully laminar jets (Zaman 1985*a*; Bridges  
 897 & Hussain 1987; Bogey & Bailly 2010; Bogey *et al.* 2012*b*). Nevertheless, they bear  
 898 significant similarities with the results obtained for the jets exhausting from the ASME  
 899 and the conical nozzles (Viswanathan & Clark 2004; Zaman 2012; Karon & Ahuja 2013).  
 900 Indeed, approximately 2 dB more noise is emitted in the first case, which was attributed  
 901 by Zaman (2012) to the fact that the exit boundary layers are nominally laminar with  
 902 the ASME nozzle, but turbulent with the conical nozzle. This hypothesis was further  
 903 supported by Karon & Ahuja (2013) who measured lower boundary-layer shape factors  
 904 for the conical nozzle and found, for instance,  $H = 2.34$  in the ASME case but  $H = 1.71$   
 905 in the conical case for  $M = 0.4$ , as indicated in table 1. The difference in noise level between  
 906 the ASME and the conical nozzles is maximum at frequencies typically one decade higher  
 907 than the jet noise peak frequencies, and is stronger for  $\phi = 90^\circ$  than for  $\phi = 30^\circ$ . Neither  
 908 of these trends are observed in this work. This may be due to the thick boundary layers  
 909 in the simulations, yielding a peak Strouhal number of only  $St_D = 1.20$  early on in the  
 910 shear layers of jetBL. By making the boundary-layer/shear-layer transition happen over  
 911 a distance of  $5r_0 - 6r_0$  for jetBL, the thick exit velocity profiles also allow the effects of  
 912 the boundary-layer shape on the mixing-layer turbulent structures to persist, as pointed  
 913 out in section 3.3.2, down to the end of the potential core, where low-frequency sound  
 914 waves are radiated in the downstream direction. Thus, it can be assumed that with a  
 915 thinner boundary layer, the extra noise components for the jet with a laminar nozzle-exit  
 916 mean velocity profile would emerge at higher frequencies, and would be lower for small  
 917 emission angles, leading to a better agreement with the ASME case.

#### 918 4. Conclusion

919 The influence of the nozzle-exit velocity profile has been investigated for isothermal  
 920 round jets at a Mach number of  $M = 0.9$  and a Reynolds number of  $Re_D = 5 \times 10^4$   
 921 with boundary-layer momentum thicknesses of 2.8% of the jet radius and peak turbu-  
 922 lence intensities of 6% at the exit of pipe nozzle. One jet with a laminar boundary-layer  
 923 profile of shape factor  $H = 2.29$  and two jets with transitional profiles with  $H = 1.71$

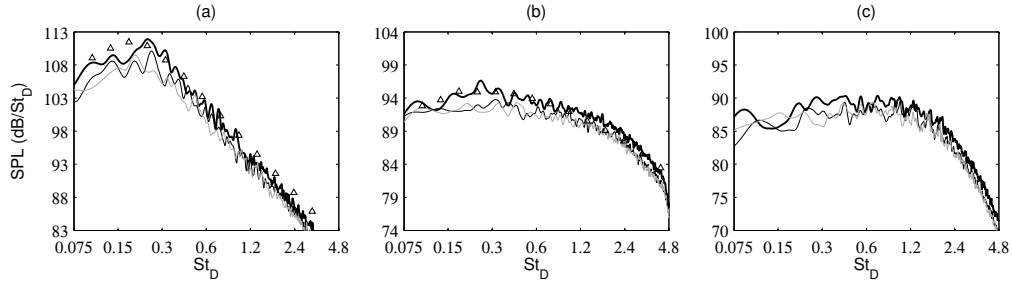


FIGURE 27. Sound pressure levels obtained at  $150r_0$  from the nozzle exit for (a)  $\phi = 30^\circ$ , (b)  $\phi = 90^\circ$  and (c)  $\phi = 150^\circ$ , as a function of  $St_D$ : — jetBL, - - - jetT1, ···· jetT2;  $\triangle$  measurements of Bridges & Brown (2005) for an isothermal jet at  $M = 0.9$  and  $Re_D = 10^6$ .

924 and 1.96 are considered. The jet flow and sound fields computed for the laminar profile  
 925 differ significantly from those for the two transitional profiles. The latter ones are very  
 926 close to each other, suggesting that similar results would be obtained for a turbulent  
 927 profile. In the non-laminar cases, the jets develop more slowly, the turbulence intensities  
 928 are lower in the mixing layers but also just downstream of the jet potential core, and less  
 929 noise is emitted in the acoustic field. Due to the sharper velocity gradient very near the  
 930 nozzle, the initial shear-layer instability waves also grow more rapidly and at higher fre-  
 931 quencies, in agreement with the predictions of a linear stability analysis performed from  
 932 the simulation profiles. Compared to the peak unstable frequencies in a mixing layer  
 933 of same momentum thickness, these frequencies are similar for the jet with a laminar  
 934 boundary-layer profile, but greater for the two other ones. As a result, the initial insta-  
 935 bility waves persist over a larger distance in the laminar case, organizing the flow and  
 936 leading to stronger large-scale structures downstream of the boundary-layer/mixing-layer  
 937 transition, than in the non-laminar cases.

938 By combining high-fidelity computations of jets with well-controlled upstream condi-  
 939 tions and linear stability analyses, this study suggests explanations for and connections  
 940 between some flow and acoustic features of free shear flows and jets, which have observed  
 941 experimentally for years or even decades but whose reasons are still unclear. This is the  
 942 case for the discrepancy in frequency of the initial instability waves between initially  
 943 laminar and initially turbulent conditions. The present results show that this discrep-  
 944 ancy is due to the fact that the most unstable frequencies near the nozzle are fixed by  
 945 the maximum velocity gradient and not by the boundary-layer momentum thickness.  
 946 Concerning the controversial issue of the persistence of coherent structures in turbulent  
 947 mixing layers, it is found that that such structures are more likely to form for a lam-  
 948 inar boundary-layer profile than for a non-laminar profile, because of the continuity of  
 949 the peak instability-wave frequencies during the changeover from a boundary-layer to a  
 950 mixing-layer profile in the first case, but of their significant decrease in the other one.  
 951 Thus, it becomes easier to understand why for some nozzles such as the ASME nozzle, at  
 952 the exit of which the flow is highly disturbed but the mean velocity profile is laminar, in-  
 953 tense large-scale structures appear in the mixing layers and additional noise is measured  
 954 in the acoustic field.

955 In this paper, in order to ensure a high numerical accuracy at a reasonable compu-  
 956 tational cost, the effects of the boundary-layer velocity profile have been investigated  
 957 for a jet at a Reynolds number only of  $Re_D = 5 \times 10^4$  with thick boundary layers. Of  
 958 course, it would be interesting to consider jets at higher Reynolds numbers with thinner  
 959 boundary layers in further simulations to get closer to the conditions encountered in the

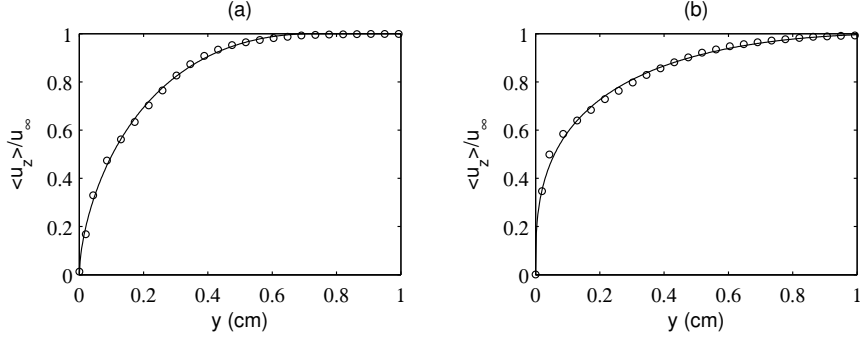


FIGURE 28. Representation of boundary-layer mean velocity profiles measured by Schubauer & Klebanoff (1955) close to the laminar-turbulent transition and of profiles given by equation (2.2) with  $y = r_0 - r$ : (a)  $\circ$  measurements at  $x = 1.91$  m and  $\text{—}$  profile T1 with  $\delta_{T_1} = 0.73$  cm, (b)  $\circ$  measurements at  $x = 2.06$  m and  $\text{—}$  profile T2 with  $\delta_{T_2} = 1.17$  cm.

laboratory-scale experiments of the literature. New experiments detailing the shear-layer  
turbulence properties just downstream of the nozzle for laminar and turbulent nozzle-exit  
velocity profiles would also be a useful complement of the present work.

### Acknowledgments

This work was granted access to the HPC resources of FLMSN (Fédération Lyonnaise de Modélisation et Sciences Numériques), partner of EQUIPEX EQUIP@MESO, and of the resources of CINES (Centre Informatique National de l'Enseignement Supérieur) and IDRIS (Institut du Développement et des Ressources en Informatique Scientifique) under the allocation 2018-2a0204 made by GENCI (Grand Equipement National de Calcul Intensif). It was performed within the framework of the Labex CeLyA of Université de Lyon, within the programme 'Investissements d'Avenir' (ANR-10-LABX-0060/ANR-16-IDEX-0005) operated by the French National Research Agency (ANR).

### Appendix A

In the simulations of jetT1 and jetT2, the axial velocity profiles T1 and T2 given by equation (2.2) with  $i = 1$  and 2 are imposed at the pipe-nozzle inlet at  $z = -2r_0$ . Considering the strong similarities between the near-wall mean-flow statistics obtained for turbulent pipe and boundary layer flows (Monty *et al.* 2009), they have been designed to fit the experimental data provided by Schubauer & Klebanoff (1955) for a boundary layer over a flat plate in the region of laminar-turbulent flow transition at two axial positions. For the comparison, the measured profiles and the T1 and T2 profiles are represented in figure 28 as a function of the distance to the wall as in the experiment, using the boundary-layer thicknesses of  $\delta_{T_1} = 0.73$  cm and  $\delta_{T_2} = 1.17$  cm in equation (2.2). In both cases, a very good agreement is observed close to the wall as well as far away from it.

### Appendix B

In a preliminary grid-sensitivity study, simulations of jetT1 and jetT2 have been performed using two grids extending in the axial direction, excluding the outflow sponge zones, only down to  $z = 4r_0$  in order to save computational time. The coarsest of the



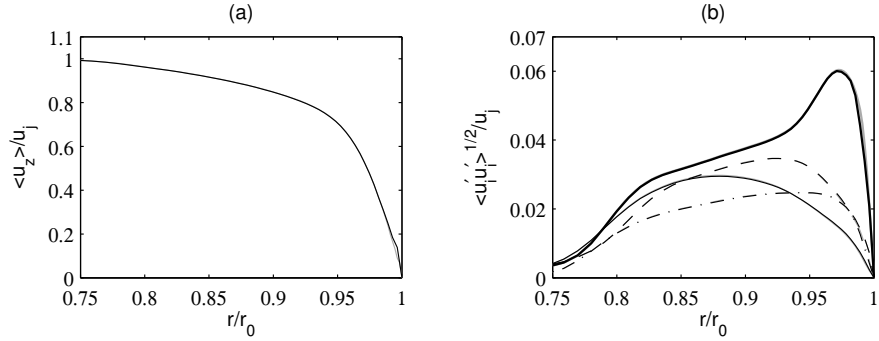


FIGURE 29. Nozzle-exit profiles (a) of mean axial velocity  $\langle u_z \rangle$  and (b) of turbulence intensities  $\langle u_z'^2 \rangle^{1/2} / u_j$ ,  $\langle u_r'^2 \rangle^{1/2} / u_j$ ,  $\langle u_\theta'^2 \rangle^{1/2} / u_j$  and  $\langle u_r' u_z' \rangle^{1/2} / u_j$  obtained for jetT2 using (black)  $\Delta r / r_0 = 0.36\%$  and (grey)  $\Delta r / r_0 = 0.18\%$  at  $r = r_0$ .

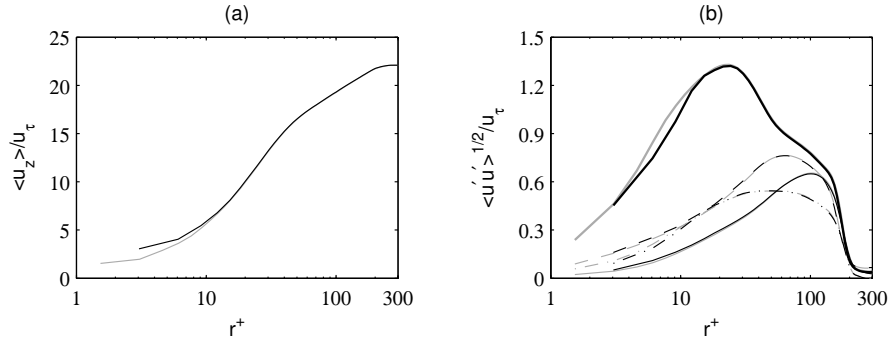


FIGURE 30. Nozzle-exit profiles (a) of mean axial velocity and (b) of turbulence intensities, represented in wall units based on the wall friction velocity using the same linetypes as in figure 29.

988 two grids coincides with the grid used for the full jet LES, defined in table 3, in the  
 989 boundary-layer region. The finest grid is identical to the coarsest one in the directions  $\theta$   
 990 and  $z$ , but differs in the radial direction with  $\Delta r / r_0 = 0.18\%$  instead of  $\Delta r / r_0 = 0.36\%$  at  
 991  $r = r_0$ . In the two additional LES, the tripping procedure is exactly the same as in the jet  
 992 LES. In the LES using the finest grid, however, the time step is twice as small because  
 993 of the numerical stability condition, leading to an application of the relaxation filtering  
 994 that is twice as frequent. The flow properties obtained using the two different grids  
 995 at the nozzle exit are found to be nearly identical. Consequently, they depend neither  
 996 on the wall-normal spacing, nor on the explicit filtering applied to remove grid-to-grid  
 997 oscillations as well as to relax subgrid-scale turbulent energy.

998 By way of illustration, the nozzle-exit profiles of mean axial velocity and of turbulence  
 999 intensities obtained for jetT2, that is for the jet with the sharpest boundary-layer profile,  
 1000 are represented in figure 29 using outer units and in figure 30 using wall units. The  
 1001 solutions calculated using the two grids with  $\Delta r / r_0 = 0.36\%$  and  $\Delta r / r_0 = 0.18\%$  at the  
 1002 wall superpose or are very close to each other.

#### REFERENCES

- 1003 AHUJA, K. K., TESTER, B. J. & TANNA, H. K. 1987 Calculation of far field jet noise spectra  
 1004 from near field measurements with true source location. *J. Sound Vib.* **116** (3), 415–426.

- 1005 ARNDT, R. E. A., LONG, D. F. & GLAUSER, M. N. 1997 The proper orthogonal decomposition  
1006 of pressure fluctuations surrounding a turbulent jet. *J. Fluid Mech.* **340**, 1–33.
- 1007 BERLAND, J., BOGEY, C., MARSDEN, O. & BAILLY, C. 2007 High-order, low dispersive and  
1008 low dissipative explicit schemes for multi-scale and boundary problems. *J. Comput. Phys.*  
1009 **224** (2), 637–662.
- 1010 BOGEY, C. 2018 Grid sensitivity of flow field and noise of high-reynolds-number jets computed  
1011 by large-eddy simulation. *Int. J. Aeroacoust.* **17** (4-5), 399–424.
- 1012 BOGEY, C. 2019 On noise generation in low reynolds number temporal round jets at a mach  
1013 number of 0.9. *J. Fluid Mech.* **859**, 1022–1056.
- 1014 BOGEY, C. & BAILLY, C. 2002 Three-dimensional non reflective boundary conditions for acous-  
1015 tic simulations: far-field formulation and validation test cases. *Acta Acust. united Ac.* **88** (4),  
1016 463–471.
- 1017 BOGEY, C. & BAILLY, C. 2004 A family of low dispersive and low dissipative explicit schemes  
1018 for flow and noise computations. *J. Comput. Phys.* **194** (1), 194–214.
- 1019 BOGEY, C. & BAILLY, C. 2006 Large eddy simulations of transitional round jets: influence of the  
1020 reynolds number on flow development and energy dissipation. *Phys. Fluids* **18** (6), 065101.
- 1021 BOGEY, C. & BAILLY, C. 2007 An analysis of the correlations between the turbulent flow and  
1022 the sound pressure field of subsonic jets. *J. Fluid Mech.* **583**, 71–97.
- 1023 BOGEY, C. & BAILLY, C. 2009 Turbulence and energy budget in a self-preserving round jet:  
1024 direct evaluation using large-eddy simulation. *J. Fluid Mech.* **627**, 129–160.
- 1025 BOGEY, C. & BAILLY, C. 2010 Influence of nozzle-exit boundary-layer conditions on the flow  
1026 and acoustic fields of initially laminar jets. *J. Fluid Mech.* **663**, 507–539.
- 1027 BOGEY, C., BARRÉ, S. & BAILLY, C. 2008 Direct computation of the noise generated by  
1028 subsonic jets originating from a straight pipe nozzle. *Int. J. Aeroacoust.* **7** (1), 1–22.
- 1029 BOGEY, C., BARRÉ, S., FLEURY, V., BAILLY, C. & JUVÉ, D. 2007 Experimental study of the  
1030 spectral properties of near-field and far-field jet noise. *Int. J. Aeroacoust.* **6** (2), 73–92.
- 1031 BOGEY, C., BARRÉ, S., JUVÉ, D. & BAILLY, C. 2009a Simulation of a hot coaxial jet: direct  
1032 noise prediction and flow-acoustics correlations. *Phys. Fluids* **21** (3), 035105.
- 1033 BOGEY, C., DE CACQUERAY, N. & BAILLY, C. 2009b A shock-capturing methodology based  
1034 on adaptative spatial filtering for high-order non-linear computations. *J. Comput. Phys.*  
1035 **228** (5), 1447–1465.
- 1036 BOGEY, C., DE CACQUERAY, N. & BAILLY, C. 2011a Finite differences for coarse azimuthal dis-  
1037 cretization and for reduction of effective resolution near origin of cylindrical flow equations.  
1038 *J. Comput. Phys.* **230** (4), 1134–1146.
- 1039 BOGEY, C. & MARSDEN, O. 2013 Identification of the effects of the nozzle-exit boundary-layer  
1040 thickness and its corresponding reynolds number in initially highly disturbed subsonic jets.  
1041 *Phys. Fluids* **25** (5), 055106.
- 1042 BOGEY, C. & MARSDEN, O. 2016 Simulations of initially highly disturbed jets with experiment-  
1043 like exit boundary layers. *AIAA J.* **54** (4), 1299–1312.
- 1044 BOGEY, C., MARSDEN, O. & BAILLY, C. 2011b Large-eddy simulation of the flow and acoustic  
1045 fields of a reynolds number  $10^5$  subsonic jet with tripped exit boundary layers. *Phys. Fluids*  
1046 **23** (3), 035104.
- 1047 BOGEY, C., MARSDEN, O. & BAILLY, C. 2011c On the spectra of nozzle-exit velocity distur-  
1048 bances in initially nominally turbulent jets. *Phys. Fluids* **23** (9), 091702.
- 1049 BOGEY, C., MARSDEN, O. & BAILLY, C. 2012a Effects of moderate reynolds numbers on  
1050 subsonic round jets with highly disturbed nozzle-exit boundary layers. *Phys. Fluids* **24** (10),  
1051 105107.
- 1052 BOGEY, C., MARSDEN, O. & BAILLY, C. 2012b Influence of initial turbulence level on the flow  
1053 and sound fields of a subsonic jet at a diameter-based reynolds number of  $10^5$ . *J. Fluid*  
1054 *Mech.* **701**, 352–385.
- 1055 BRADSHAW, P. 1966 The effect of initial conditions on the development of a free shear layer. *J.*  
1056 *Fluid Mech.* **26** (2), 225–236.
- 1057 BRÈS, G. A., JORDAN, P., JAUNET, V., LE RALLIC, M., CAVALIERI, A. V. G., TOWNE,  
1058 A., LELE, S. K., COLONIUS, T. & SCHMIDT, O. T. 2018 Importance of the nozzle-exit  
1059 boundary-layer state in subsonic turbulent jets. *J. Fluid Mech.* **851**, 83–124.
- 1060 BRIDGES, J. & BROWN, C. A. 2005 Validation of the small hot jet acoustic rig for aeroacoustics.  
1061 *Tech. Rep.* 2005-2846. AIAA Paper.

- 1062 BRIDGES, J. E. & HUSSAIN, A. K. M. F. 1987 Roles of initial conditions and vortex pairing in  
1063 jet noise. *J. Sound Vib.* **117** (2), 289–311.
- 1064 BROWAND, F. K. & LATIGO, B. O. 1979 Growth of the two-dimensional mixing layer from a  
1065 turbulent and nonturbulent boundary layer. *Phys. Fluids* **22** (6), 1011–1019.
- 1066 BROWN, G. L. & ROSHKO, A. 1974 On density effects and large structure in turbulent mixing  
1067 layers. *J. Fluid Mech.* **64** (4), 775–816.
- 1068 BÜHLER, S., KLEISER, L. & BOGEY, C. 2014 Simulation of subsonic turbulent nozzle-jet flow  
1069 and its near-field sound. *AIAA J.* **52** (8), 1653–1669.
- 1070 CASTELAIN, T. 2006 Contrôle de jet par microjets impactants. Mesure de bruit rayonné et  
1071 analyse aérodynamique. PhD thesis, Ecole Centrale de Lyon, France, no. 2006-33.
- 1072 CASTILLO, L. & JOHANSSON, T. G. 2012 The effects of the upstream conditions on a low  
1073 reynolds number turbulent boundary layer with zero pressure gradient. *J. Turbul.* **3**, 031.
- 1074 CAVALIERI, A. V. G., JORDAN, P., COLONIUS, T. & GERVAIS, Y. 2012 Axisymmetric superdi-  
1075 rectivity in subsonic jets. *J. Fluid Mech.* **704**, 388–420.
- 1076 CHANDRSUDA, C., MEHTA, R. D., WEIR, A. D. & BRADSHAW, P. 1978 Effect of free-stream  
1077 turbulence on large structure in turbulent mixing layers. *J. Fluid Mech.* **85** (4), 693–704.
- 1078 CHU, W. T. & KAPLAN, R. E. 1976 Use of a spherical concave reflector for jet-noise-source  
1079 distribution diagnosis. *J. Acoust. Soc. Am.* **59** (6), 1268–1277.
- 1080 COLES, D. E. 1962 The turbulent boundary layer in a compressible fluid. *Tech. Rep.* R-403-PR.  
1081 Rand Corp.
- 1082 CRIGHTON, D. G. 1981 Acoustics as a branch of fluid mechanics. *J. Fluid Mech.* **106**, 261–298.
- 1083 CROW, S. C. & CHAMPAGNE, F. H. 1971 Orderly structure in jet turbulence. *J. Fluid Mech.*  
1084 **48**, 547–591.
- 1085 DE CHANT, L. J. 2005 The venerable 1/7th power law turbulent velocity profile: a classical  
1086 nonlinear boundary value problem solution and its relationship to stochastic processes.  
1087 *Appl. Math. Comput.* **161** (2), 463–474.
- 1088 DRUBKA, R. E. & NAGIB, H. M. 1981 Instabilities in near field of turbulent jets and their  
1089 dependence on initial conditions and reynolds number. *Tech. Rep.* R-81-2. IIT Fluids &  
1090 Heat Transfer Report.
- 1091 ERM, P. L. & JOUBERT, P. N. 1991 Low-reynolds-number turbulent boundary layers. *J. Fluid  
1092 Mech.* **230**, 1–44.
- 1093 FAUCONNIER, D., BOGEY, C. & DICK, E. 2013 On the performance of relaxation filtering for  
1094 large-eddy simulation. *J. Turbulence* **14** (1), 22–49.
- 1095 FERNHOLZ, H. H. & FINLEY, P. J. 1996 The incompressible zero-pressure-gradient turbulent  
1096 boundary layer: an assessment of the data. *Prog. Aerosp. Sci.* **32** (4), 245–311.
- 1097 FIELDLER, H. E. 1988 Coherent structures in turbulent flows. *Prog. Aerosp. Sci.* **25**, 231–269.
- 1098 FISHER, M. J., HARPER-BOURNE, M. & GLEGG, S. A. L. 1977 Jet engine noise source location:  
1099 The polar correlation technique. *J. Sound Vib.* **51** (1), 23–54.
- 1100 FLEURY, V. 2006 Superdirectivité, bruit d'appariement et autres contributions au bruit de jet  
1101 subsonique. PhD thesis, Ecole Centrale de Lyon, France, no. 2006-18.
- 1102 FLEURY, V., BAILLY, C., JONDEAU, E., MICHARD, M. & JUVÉ, D. 2008 Space-time correlations  
1103 in two subsonic jets using dual-piv measurements. *AIAA J.* **46** (10), 2498–2509.
- 1104 FONTAINE, R. A., ELLIOTT, G. S., AUSTIN, J. M. & FREUND, J. B. 2015 Very near-nozzle  
1105 shear-layer turbulence and jet noise. *J. Fluid Mech.* **770**, 27–51.
- 1106 GLOERFELT, X. & BERLAND, J. 2012 Turbulent boundary layer noise: direct radiation at mach  
1107 number 0.5. *J. Fluid Mech.* **723**, 318–351.
- 1108 GUTMARK, E. & HO, C.-M. 1983 Preferred modes and the spreading rates of jets. *Phys. Fluids*  
1109 **26** (10), 2932–2938.
- 1110 HARPER-BOURNE, M. 2010 Jet noise measurements: past and present. *Int. J. Aeroacoust.*  
1111 **9** (4 & 5), 559–588.
- 1112 HILL, W. G., JENKINS, R. C. & GILBERT, B. L. 1976 Effects of the initial boundary-layer state  
1113 on turbulent jet mixing. *AIAA J.* **14** (11), 1513–1514.
- 1114 HO, C. & HUERRE, P. 1984 Perturbed free shear layers. *Annu. Rev. Fluid Mech.* **16**, 365–422.
- 1115 HUSAIN, Z. D. & HUSSAIN, A. K. M. F. 1979 Axisymmetric mixing layer: influence of the  
1116 initial and boundary conditions. *AIAA J.* **17** (1), 48–55.
- 1117 HUSSAIN, A. K. M. F. 1986 Coherent structures and turbulence. *J. Fluid Mech.* **173**, 303–356.

- 1118 HUSSAIN, A. K. M. F. & ZAMAN, K. B. M. Q. 1985 An experimental study of organized  
1119 motions in the turbulent plane mixing layer. *J. Fluid Mech.* **159**, 85–104.
- 1120 HUSSAIN, A. K. M. F. & ZEDAN, M. F. 1978*a* Effects of the initial condition on the axisymmet-  
1121 ric free shear layer: Effects of the initial fluctuation level. *Phys. Fluids* **21** (9), 1475–1481.
- 1122 HUSSAIN, A. K. M. F. & ZEDAN, M. F. 1978*b* Effects of the initial condition on the axisymmetric  
1123 free shear layer: Effects of the initial momentum thickness. *Phys. Fluids* **21** (7), 1100–1112.
- 1124 HUTCHINGS, N. 2012 Caution: tripping hazards. *J. Fluid Mech.* **710**, 1–4.
- 1125 KARON, A. Z. & AHUJA, K. K. 2013 Effect of nozzle-exit boundary layer on jet noise. *Tech.*  
1126 *Rep.* 2013-0615. AIAA Paper.
- 1127 KIM, J., MOIN, P., & MOSER, R. 1987 Turbulence statistics in fully developed channel flow at  
1128 low reynolds number. *J. Fluid Mech.* **177**, 133–166.
- 1129 KLEBANOFF, P. S. & DIEHL, Z. W. 1952 Some features of artificially thickened fully developed  
1130 turbulent boundary layers with zero pressure gradient. *Tech. Rep.* 1110. NACA TN.
- 1131 KREMER, F. & BOGEY, C. 2015 Large-eddy simulation of turbulent channel flow using relaxation  
1132 filtering: resolution requirement and reynolds number effects. *Comput. Fluids* **116**, 17–28.
- 1133 LAU, J. C., MORRIS, P. J. & FISHER, M. J. 1979 Measurements in subsonic and supersonic  
1134 free jets using a laser velocimeter. *J. Fluid Mech.* **93** (1), 1–27.
- 1135 LEE, S. S. & BRIDGES, J. 2005 Phased-array measurements of single flow hot jets. *Tech. Rep.*  
1136 2005-213826. NACA TM.
- 1137 LILLEY, G. M. 1994 Jet noise classical theory and experiments. In *Aeroacoustics of Flight*  
1138 *Vehicles* (ed. H. H. Hubbard), , vol. 1, pp. 211—289. Acoustical Society of America.
- 1139 LORTEAU, M., CLÉRO, F. & VUILLOT, F. 2015 Analysis of noise radiation mechanisms in hot  
1140 subsonic jet from a validated large eddy simulation solution. *Phys. Fluids* **27** (7), 075108.
- 1141 MAESTRELLO, L. & MCDAID, E. 1971 Acoustic characteristics of a high-subsonic jet. *AIAA J.*  
1142 **9** (6), 1058–1066.
- 1143 MICHALKE, A. 1984 Survey on jet instability theory. *Prog. Aerosp. Sci.* **21**, 159–199.
- 1144 MOHSENI, K. & COLONIUS, T. 2000 Numerical treatment of polar coordinate singularities. *J.*  
1145 *Comput. Phys.* **157** (2), 787–795.
- 1146 MOLLO-CHRISTENSEN, E., KOLPIN, M. A. & MARTUCELLI, J. R. 1964 Experiments on jet flows  
1147 and jet noise far-field spectra and directivity patterns. *J. Fluid Mech.* **18** (2), 285–301.
- 1148 MONTY, J. P., HUTCHINS, N., NG, H. C. H., MARUSIC, I. & CHONG, M. S. 2009 A comparison  
1149 of turbulent pipe, channel and boundary layer flows. *J. Fluid Mech.* **632**, 431–442.
- 1150 MORRIS, P. J. 1976 The spatial viscous instability of axisymmetric jets. *J. Fluid Mech.* **77** (3),  
1151 511–529.
- 1152 MORRIS, P. J. 2010 The instability of high speed jets. *Int. J. Aeroacoust.* **9** (1-2), 1–50.
- 1153 MORRIS, P. J. & ZAMAN, K. B. M. Q. 2009 Velocity measurements in jets with application to  
1154 noise source modelling. *J. Sound Vib.* **329** (4), 394–414.
- 1155 MORRIS, S. C. & FOSS, J. F. 2003 Turbulent boundary layer to single-stream shear layer: the  
1156 transition region. *J. Fluid Mech.* **494**, 187–221.
- 1157 NARAYANAN, S., BARBER, T. J. & POLAK, D. R. 2002 High subsonic jet experiments: Turbu-  
1158 lence and noise generation studies. *AIAA J.* **40** (3), 430–437.
- 1159 PANDA, J., SEASHOLTZ, R. G. & ELAM, K. A. 2005 Investigation of noise sources in high-speed  
1160 jets via correlation measurements. *J. Fluid Mech.* **537**, 349–385.
- 1161 RAMAN, G., RICE, E. J. & RESHOTKO, E. 1994 Mode spectra of natural disturbances in a  
1162 circular jet and the effect of acoustic forcing. *Exp. Fluids* **17**, 415–426.
- 1163 RAMAN, G., ZAMAN, K. B. M. Q. & RICE, E. J. 1989 Initial turbulence effect on jet evolution  
1164 with and without tonal excitation. *Phys. Fluids A* **1** (7), 1240–1248.
- 1165 RUSS, S. & STRYKOWSKI, P. J. 1993 Turbulent structure and entrainment in heated jets: The  
1166 effect of initial conditions. *Phys. Fluids A* **5** (12), 3216–3225.
- 1167 SABATINI, R. & BAILLY, C. 2015 Numerical algorithm for computing acoustic and vortical  
1168 spatial instability waves. *AIAA J.* **53** (3), 692–702.
- 1169 SANDBERG, R. D., SANDHAM, N. D. & SUPONITSKY, V. 2012 DNS of compressible pipe flow  
1170 exiting into a coflow. *Int. J. Heat and Fluid Flow* **35**, 33–44.
- 1171 SATO, H. 1971 Experimental investigation on the transition of laminar separated layer. *J. Phys.*  
1172 *Soc. Jpn.* **48**, 702–709.

- 1173 SCHLATTER, P. & ÖRLÜ, R. 2012 Turbulent boundary layers at moderate reynolds numbers:  
1174 inflow length and tripping effects. *J. Fluid Mech.* **710**, 5–34.
- 1175 SCHUBAUER, G. B. & KLEBANOFF, P. S. 1955 Contributions on the mechanics of boundary-  
1176 layer transition. *Tech. Rep.* 3498. NACA TN.
- 1177 SPALART, P. R. 1988 Direct simulation of a turbulent boundary layer up to  $r_\theta = 1410$ . *J. Fluid*  
1178 *Mech.* **187**, 61–98.
- 1179 TAM, C. K. W. 1998 Jet noise: Since 1952. *Theor. Comput. Fluid Dyn.* **10** (1-4), 393–405.
- 1180 TAM, C. K. W. & DONG, Z. 1996 Radiation and outflow boundary conditions for direct com-  
1181 putation of acoustic and flow disturbances in a nonuniform mean flow. *J. Comput. Acous.*  
1182 **4** (2), 175–201.
- 1183 TAM, C. K. W., VISWANATHAN, K., AHUJA, K. K. & PANDA, J. 2008 The sources of jet noise:  
1184 experimental evidence. *J. Fluid Mech.* **615**, 253–292.
- 1185 TANNA, H. K. 1977 An experimental study of jet noise. part i: Turbulent mixing noise. *J. Sound*  
1186 *Vib.* **50** (3), 405–428.
- 1187 TOMKINS, C. D. & ADRIAN, R. J. 2005 Energetic spanwise modes in the logarithmic layer of  
1188 a turbulent boundary layer. *J. Fluid Mech.* **545**, 141–162.
- 1189 UZUN, A. & HUSSAINI, M. 2007 Investigation of high frequency noise generation in the near-  
1190 nozzle region of a jet using large eddy simulation. *Theor. Comput. Fluid Dyn.* **21** (4),  
1191 291–321.
- 1192 VISWANATHAN, K. 2004 Aeroacoustics of hot jets. *J. Fluid Mech.* **516**, 39–82.
- 1193 VISWANATHAN, K. 2006 Distributions of noise sources in heated and cold jets: are they different?  
1194 *Int. J. Aeroacoust.* **9** (4 & 5), 589–626.
- 1195 VISWANATHAN, K. & CLARK, L. T. 2004 Effect of nozzle internal contour on jet aeroacoustics.  
1196 *Int. J. Aeroacoust.* **3** (2), 103–135.
- 1197 WYGNANSKI, I., OSTER, D., FIEDLER, H. & DZIOMBA, B. 1979 On the perseverance of a  
1198 quasi-two-dimensional eddy-structure in a turbulent mixing layer. *J. Fluid Mech.* **93** (2),  
1199 325–335.
- 1200 XU, G. & ANTONIA, R. A. 2002 Effects of different initial conditions on a turbulent free jet.  
1201 *Exp. Fluids* **33**, 677–683.
- 1202 YULE, A. J. 1978 Large-scale structure in the mixing layer of a round jet. *J. Fluid Mech.* **89** (3),  
1203 413–432.
- 1204 ZAMAN, K. B. M. Q. 1985a Effect of initial condition on subsonic jet noise. *AIAA J.* **23** (9),  
1205 1370–1373.
- 1206 ZAMAN, K. B. M. Q. 1985b Far-field noise of a subsonic jet under controlled excitation. *J. Fluid*  
1207 *Mech.* **152**, 83–111.
- 1208 ZAMAN, K. B. M. Q. 1986 Flow field and near and far sound field of a subsonic jet. *J. Sound*  
1209 *Vib.* **106** (1), 1–16.
- 1210 ZAMAN, K. B. M. Q. 2012 Effect of initial boundary-layer state on subsonic jet noise. *AIAA J.*  
1211 **50** (8), 1784–1795.
- 1212 ZAMAN, K. B. M. Q. 2017 Increased jet noise due to a "nominally laminar" state of nozzle exit  
1213 boundary layer. *Tech. Rep.* 2017-219440. NASA TM.
- 1214 ZAMAN, K. B. M. Q. & HUSSAIN, A. K. M. F. 1981 Turbulence suppression in free shear flows  
1215 by controlled excitation. *J. Fluid Mech.* **103**, 133–159.
- 1216 ZHU, M., PÉREZ ARROYO, C., FOSSO POUANGUÉ, A., SANJOSÉ, M. & MOREAU, S. 2018  
1217 Isothermal and heated subsonic jet noise using large eddy simulations on unstructured  
1218 grids. *Comput. Fluids* **171**, 166–192.